Journal of Computational Physics 394 (2019) 18–40

Contents lists available at ScienceDirect

Journal of Computational Physics

www.elsevier.com/locate/jcp

Application of CE/SE method to gas-particle two-phase detonations under an Eulerian-Lagrangian framework

Zijian Zhang [a,c], Chihyung Wen [b], Yunfeng Liu [a,c,*], Deliang Zhang [c], Zonglin Jiang [a,c]

[a] School of Engineering Science, University of Chinese Academy of Sciences, Beijing 100049, China
[b] Department of Mechanical Engineering, The Hong Kong Polytechnic University, Kowloon, Hong Kong
[c] Institute of Mechanics, Chinese Academy of Sciences, Beijing 100190, China

ARTICLE INFO

Article history:
Received 18 December 2018
Received in revised form 3 May 2019
Accepted 19 May 2019
Available online 22 May 2019

Keywords:
Two-phase detonation
CE/SE
Eulerian-Lagrangian
MPI
Aluminum-air detonation

ABSTRACT

This study aims to extend the original Eulerian space-time conservation element and solution element (CE/SE) method to the Eulerian-Lagrangian framework to solve the gas-particle two-phase detonation problems. The gas-aluminum particle two-phase detonations are numerically investigated by the developed Eulerian-Lagrangian code, in which the gas-phase compressible Euler equations are solved by our in-house CE/SE scheme based on quadrilateral meshes. Additionally, the particle-phase Lagrangian equations, together with the stiff source terms of interphase interactions and chemical reactions, are explicitly integrated via the operator-splitting technique. A dynamic data structure is introduced to store particle information to overcome the tremendous communication costs when applying message passing interface parallel to the Eulerian-Lagrangian framework. The code is shown to be of better parallel efficiency in moderate-scale computations than that uses static arrays. Comparisons with previous one-dimensional and two-dimensional simulation results and experimental observations are conducted to demonstrate the accuracy and reliability of the developed Eulerian-Lagrangian CE/SE code in gas-particle two-phase detonation simulations. Moreover, the code is also applied to simulate poly-disperse gas-particle detonations which is close to a realistic scenario, and significant differences in detonation characteristics are found when compared with the monodisperse counterparts. The great demands of using the Eulerian-Lagrangian method to obtain more physics-consistent gas-particle detonation results are addressed, which the traditional Eulerian-Eulerian simulations fail to observe.

© 2019 Elsevier Inc. All rights reserved.

1. Introduction

When fine reactive powder, produced and used in many factories, is suspended cumulatively in an oxidizing atmosphere, such as air or oxygen (O_2), it bears a potential danger of ignition and further development into detonation, leading to severe financial losses, personnel injuries and fatalities [1,2]. On the other hand, with the characteristics of high energy density, low detonability limit and easy storage and transportation [3], reactive solid particles (especially metal particles) are in favor for many propellant applications, such as solid rocket propellants [4,5] and, more recently, potential use for detonation in

* Corresponding author at: Institute of Mechanics, Chinese Academy of Sciences, Beijing 100190, China.
E-mail address: liuyunfeng@imech.ac.cn (Y. Liu).

https://doi.org/10.1016/j.jcp.2019.05.025
0021-9991/© 2019 Elsevier Inc. All rights reserved.

hypersonic propulsion [6]. Therefore, the study of detonation processes in reactive gas-particle two-phase mixtures is of great importance for dust explosion hazard prevention and fire safety in factories, and for advanced propulsion applications.

Some experiments involving gas-particle detonation have been reported, such as Zhang et al. [7–9], Veyssiere et al. [10], Borisov et al. [11] and Ingignoli et al. [12]. They detonated various suspensions of reactive particles, including aluminum (Al), starch, and anthraquinone particles, in air or oxygen atmospheres using different initiation sources. Findings indicated that detonation of such mixtures is only feasible when the characteristic size of particles is less than a few micrometers and it needs to be in large tubes by using strong initiation sources; therefore, it imposes greater difficulties compared with classical gaseous detonation experiments. In addition, given the dispersion problems of mixtures of suspended solid particles in gases, it is challenging to achieve well-controlled and reproducible experimental conditions. Consequently, available experimental data on detonation characteristics, structures, and detonability of solid particle-gas mixtures are still rather limited and comparison among them is difficult as well, which renders numerical simulation an important aspect of studying gas-particle detonations.

As gas-particle two-phase detonations are complex multi-physics problems involving high-speed reactive flows, mathematical models describing these types of flows are extremely complicated and still under development. Based on the classic experimental observations for combustion of large reactive particles in quiescent atmospheres [13,14], the diffusion-controlled combustion theory for droplets has often been applied to two-phase detonation problems of solid particles [15, 16]. Considering the dependence of the combustion of fine metal particles on pressure, which has been reported in experiments [9,17,18], a kinetics-controlled combustion model for gas-particle detonation was proposed by Fedorov's group [19–22]. Recently, a combination of the above two widely used models, the surface-kinetic-oxidation and diffusion hybrid reaction model was proposed by Zhang et al. [23] and has been applied in references [24,25]. All these simulation results lead to an important quantitative relationship in gas-particle detonation; that is, many characteristic lengths in two-phase detonation, such as the induction length, two-phase relaxation lengths, detonation cell size, etc. are proportional to the particle size to a power of 1.4–2. Another significant conclusion in hybrid gas-particle detonation is that the existence of reactive particles in gaseous explosive mixtures exerts unique effects on the structure and propagation of the detonation wave, depending on the particle size, and multiple detonation regimes with different velocities and structures exist in certain ranges [26,27].

Among current numerical simulations of gas-particle detonation, apart from the great progress in combustion modeling of solid particles, the methodology employed to address the multiphase high-speed reactive flow remains limited to the Eulerian-Eulerian method (EEM). The EEM is also referred to as the two-fluid model; it considers the particle phase as a continuous medium, such that continuous medium mechanics can be used to describe the motion of the particle phase which then becomes another "fluid". This is a simple and effective way to deal with the discrete phase, but some inherent limitations emerge when more realistic conditions are considered. All particles within one numerical mesh are assumed to be in the same states, such as the same particle size, temperature, velocity and so on. However, the number of particles within one mesh may be large, and their states may differ depending on their initial states and history of interactions. For example, the particles involved in industries or experiments are always characterized by a specific particle size distribution, with a relatively wide range of particle diameters [5,9,23]. Also, as known, the forces acted upon and the heat transferred to particles from the gases in two-phase flows differ by the particle size, which results in different temperatures and velocities of particles within one mesh. Moreover, as mentioned above, many characteristics of gas-particle two-phase detonation are significantly influenced by the particle size. Consequently, in light of these various limitations, the EEM is evidently insufficient to reflect the true physics of gas-particle detonations and to simulate them accurately.

In the modeling of multiphase low-speed incompressible flows, another discrete phase method, the Eulerian-Lagrangian method (ELM), is often used [28,29]. The ELM tracks every Lagrangian particle in the condensed phase by Newton's laws of motion, allowing for the states of every particle to be solved individually. The ELM seems more physically reasonable in modeling gas-particle detonation, especially more capable in dealing with suspensions with particle size distributions. However, it has not been developed to solve high-speed reactive flows yet, potentially because the number of fine particles has proven too large and simulations too expensive to achieve in the past. Nowadays, with the rapid development of computer technologies, high-performance computer clusters are readily accessible, and parallel computing techniques can be applied to accelerate computation with high efficiency. Therefore, we are motivated to develop an algorithm to solve gas-particle detonation problems under an Eulerian-Lagrangian framework by using parallel computations. We intend to study gas-particle detonation in a more realistic manner. However, the application of parallel computation under an Eulerian-Lagrangian framework is not as easy as that under a purely Eulerian framework. A large amount of information exchange from one computational core to another, for calculations of the interaction source terms between two phases, leads to formidable costs in cores' communication, especially when the Eulerian framework is staggered with the Lagrangian framework due to the relative movement between these two phases. Only when this problem is solved properly can parallel computing techniques be used to accelerate computation of high-speed two-phase flows under an Eulerian-Lagrangian framework.

On the other hand, for the solution of the gaseous phase in the Eulerian framework, the conflict between stability and numerical accuracy is one of the focused issues for nearly every established method in computational fluid dynamics (CFD), especially when solving high-speed reactive flows such as detonation problems. As for two-phase reactive flows, apart from the reaction source terms, phase interactions, including forces, heat transfers and mass transfers, also exist in the source terms, which poses a greater challenge to numerical schemes [30,31]. In 1991, by using a unique approach of enforcing flux

conservation in both space and time with thorough physics considerations, Chang and To [32] developed the space-time conservation element and solution element (CE/SE) method to solve conservation laws in fluid dynamics. Thereafter, CE/SE has been demonstrated to obtain highly accurate numerical solutions for 1D, 2D and 3D flow problems involving shocks, contact discontinuities, vortices, etc. by Chang and co-workers [32–40]. Recently, the CE/SE method has been successfully extended to solve gaseous detonation problems [41–44], two-phase shock-droplet interactions [45–47] and other high-speed reactive flows [48]. A high-order CE/SE scheme with a hybrid grid has also been developed [49]. Further, Wang et al. [50,51] have successfully applied the CE/SE method to study two-phase detonation problems under an Eulerian-Eulerian framework without using parallel computing techniques. It is proven that the CE/SE method is of high accuracy and good stability in solving two-phase detonation problems, at least in the Eulerian-Eulerian framework. Therefore, the present work aims to extend the CE/SE method to solve gas-particle two-phase detonation problems under an Eulerian-Lagrangian framework using Message Passing Interface (MPI) parallel computing technique.

The remaining parts of this paper are organized as follows. The detailed descriptions about the physical models and governing equations of high-speed two-phase reactive flows under the Eulerian-Lagrangian framework are presented in Section 2, following by the introductions of the particle combustion model in Section 3, the CE/SE method in Section 4, and the two-phase MPI parallel accelerating technique in Section 5. Then, in Sections 6.1–6.3, three cases that have been reported in previous papers [23,24,31] are employed to benchmark the capacities of the developed computer code for high-speed gas-particle flow simulations, especially for gas-particle detonation problems. Finally, in Section 6.4, realistic gas-particle detonations with log-normal particle size distributions are investigated and compared with their monodisperse counterparts to showcase the superiorities of the developed Eulerian-Lagrangian code in polydisperse gas-particle detonation simulations.

2. Governing equations and physical models

In this study, gas-particle detonation is modeled under an Eulerian-Lagrangian framework. Small reactive solid particles are assumed to be spherical in shape and uniformly suspended in the oxidizing gas atmosphere. The two-phase mixture is further assumed to be diluted enough to neglect the volume fraction of solid particles and particle-particle collisions. In the highly transient two-phase flow with strong shock waves, the gas and particles are treated to be in thermal and mechanical non-equilibrium, which means that the temporal momentum exchange, heat transfer as well as mass exchange between gas and particles are updated throughout the process. Further, the temperature distribution within particles is considered uniform due to small particle sizes and reaction heat is ideally absorbed only by gas. Based on the above assumptions, the motion of gas in the two-dimensional form can be described by the unsteady, multi-species, reactive Euler equations with interphase interaction terms:

$$\frac{\partial \mathbf{U}}{\partial t}+\frac{\partial \mathbf{F}}{\partial x}+\frac{\partial \mathbf{G}}{\partial y}=\mathbf{S}+\mathbf{W}, \tag{1}$$

where $\mathbf{U}$ is the vector of conserved variables, $\mathbf{F}$ and $\mathbf{G}$ are the conservation flux vectors in the x- and y-directions, and $\mathbf{S}$ and $\mathbf{W}$ are the vectors of the gas-particle interaction and chemical reaction source terms, respectively.

$$\mathbf{U}=[\rho_1,\cdots,\rho_{ns},\rho u,\rho v,E]^{\mathrm{T}}, \tag{2}$$

$$\mathbf{F}=\left[\rho_1 u,\cdots,\rho_{ns}u,\rho u^2+p,\rho uv,(E+p)u\right]^{\mathrm{T}}, \tag{3}$$

$$\mathbf{G}=\left[\rho_1 v,\cdots,\rho_{ns}v,\rho uv,\rho v^2+p,(E+p)v\right]^{\mathrm{T}}, \tag{4}$$

$$\mathbf{S}=\frac{1}{dV}\sum_{k=1}^{np}\begin{bmatrix}0\\ \vdots\\ J_{pk}\\ \vdots\\ 0\\ -f_{xk}+u_{pk}J_{pk}\\ -f_{yk}+v_{pk}J_{pk}\\ -q_{pk}-(u_{pk}f_{xk}+v_{pk}f_{yk})+\frac{1}{2}(u_{pk}^2+v_{pk}^2)\cdot J_{pk}+e_{pk}\cdot J_{pk}\end{bmatrix}, \tag{5}$$

and

$$\mathbf{W}=[\dot{\omega}_1,\cdots,\dot{\omega}_{ns},0,0,0]^{\mathrm{T}}. \tag{6}$$

In the gas-phase equations (2)–(4), ρ_i is the mass density of species i and $i=1,\ldots,ns$; ns is the number of species contained in the gas mixture; p, u and v are the gas pressure and x- and y-components of gas velocity, respectively; and ρ and E are the mass density and total energy of the gas mixture. In Eq. (5), the subscript pk represents all the quantities

related to the kth particle. The corresponding definitions of these quantities will be detailed later when introducing the particle governing equations in this section (Eqs. (12)–(21)). To include all effects of particles into the gas source term $\mathbf{S}$, the summation is done within the small volume element dV, and np is the number of particles in dV. In Eq. (6), $\dot{\omega}_i$ for $i = 1, \ldots, ns$ is the mass production rate of gaseous species i by chemical reactions. By assuming infinitely fast reactions in the gas phase, $\dot{\omega}_i$ is only determined by the chemical reactions involved and the amounts of reactants available in the gas phase. The specific chemical reactions will be introduced in Section 6, depending on the problems considered.

The mass density ρ and total energy E of the gas mixture can be calculated by

$$\rho = \sum_{i=1}^{ns} \rho_i, \quad E = \rho h - p + \frac{1}{2}\rho\left(u^2 + v^2\right), \tag{7}$$

where h is the specific enthalpy of the gas mixture, calculated by

$$h = \sum_{i=1}^{ns} \frac{\rho_i}{\rho} h_i, \tag{8}$$

with the specific enthalpy of each individual species, h_i, obtained from the 9-coefficient (a_1–a_7, b_1 and b_2) NASA representation as a function of gas temperature T [52]:

$$\frac{h_i}{R_i T} = -a_{1i}T^{-2} + a_{2i}T^{-1}\ln T + a_{3i} + \frac{1}{2}a_{4i}T + \frac{1}{3}a_{5i}T^2 + \frac{1}{4}a_{6i}T^3 + \frac{1}{5}a_{7i}T^4 + b_{1i}T^{-1}. \tag{9}$$

In Eq. (9), R_i is the gas constant of species i and can be expressed as

$$R_i = \frac{R_0}{W_i}, \tag{10}$$

where $R_0 = 8.314$ J/(mol K) is the universal gas constant, and W_i is the molecular weight of species i. By assuming each individual species as a perfect gas, the equation of state of the gas mixture is given by

$$p = \sum_{i=1}^{ns} \rho_i R_i T. \tag{11}$$

Under the Eulerian-Lagrangian framework, the motion of every particle is tracked by Newton's laws of motion. For the kth particle, the governing equations can be written as

$$\frac{d\mathbf{L}_{pk}}{dt} = \mathbf{S}_{pk}, \tag{12}$$

where $\mathbf{L}_{pk}$ is the vector of the Lagrangian variables of the kth particle, and $\mathbf{S}_{pk}$ is the corresponding vector of the source terms. $\mathbf{L}_{pk}$ and $\mathbf{S}_{pk}$ are expressed as

$$\mathbf{L}_{pk} = [m_{pk}, x_{pk}, y_{pk}, m_{pk}u_{pk}, m_{pk}v_{pk}, E_{pk}]^{\mathrm{T}}, \tag{13}$$

and

$$\mathbf{S}_{pk} = [-J_{pk}, u_{pk}, v_{pk}, f_{xk}, f_{yk}, -e_{pk}J_{pk} + q_{pk}]^{\mathrm{T}}. \tag{14}$$

In Eqs. (13) and (14) (also in Eq. (5)), J_{pk} is the mass regression rate of the kth particle and it only contributes to the density change of the particle vapor in the gas mixture and has no contribution to other species. Particle regression is related to particle combustion; hence, J_{pk} is determined by the combustion model of the particle and referred to as the combustion rate of the particle, which will be discussed in Section 3. u_{pk} and v_{pk} are the x- and y-components of the kth particle's velocity, respectively. e_{pk} is the specific internal energy of the kth particle and can also be evaluated by Eq. (9) with particle temperature T_{pk}. For the condensed phase, the internal energy is always considered equal to the enthalpy. Notably, different sets of polynomial coefficients are chosen to evaluate the e_{pk} of different particle phases; therefore, the latent heats of phase change are automatically included. m_{pk} and E_{pk} are the mass and total internal energy of the kth particle, respectively, and $E_{pk} = m_{pk} \cdot e_{pk}$.

In addition, f_{xk} and f_{yk} are the x- and y-components of the drag force acting on the kth particle and can be modeled as follows:

$$\begin{cases} f_{xk} = \dfrac{\pi}{8} C_{Dk} d_{pk}^2 \rho |V - V_{pk}|(u - u_{pk}) \\ f_{yk} = \dfrac{\pi}{8} C_{Dk} d_{pk}^2 \rho |V - V_{pk}|(v - v_{pk}) \end{cases}, \tag{15}$$

where d_{pk} is the diameter of the particle and C_{Dk} is the drag coefficient,

$$C_{Dk} = \frac{24}{\mathrm{Re}_{pk}}\left(1 + \frac{1}{6}\mathrm{Re}_{pk}^{2/3}\right). \tag{16}$$

In Eqs. (15) and (16), the gas-particle relative velocity and the relative Reynolds number Re_{pk} can be calculated by

$$|V - V_{pk}| = \left[(u - u_{pk})^2 + (v - v_{pk})^2\right]^{1/2}, \tag{17}$$

and

$$\mathrm{Re}_{pk} = \frac{\rho d_{pk}|V - V_{pk}|}{\mu}, \tag{18}$$

where μ is the viscosity coefficient of gas and can be obtained by Sutherland's law:

$$\mu = \frac{C_1 T^{2/3}}{T + C_2}, \tag{19}$$

with $C_1 = 1.458 \times 10^{-6}$ kg/(m s) and $C_2 = 110.4$ K for air.

Accordingly, the convection heat transfer between the gas and the kth particle is expressed as follows:

$$q_{pk} = \pi d_{pk}\lambda \mathrm{Nu}_{pk}(T - T_{pk}), \tag{20}$$

with the particle Nusselt number expressed as

$$\mathrm{Nu}_{pk} = 2 + 0.459\,\mathrm{Re}_{pk}^{0.55}\,\mathrm{Pr}^{0.33}, \tag{21}$$

where $\mathrm{Pr} = 0.72$ is the Prandtl number and λ is the heat conduction coefficient of gas, calculated by

$$\lambda = \frac{C_p \mu}{\mathrm{Pr}}. \tag{22}$$

In Eq. (22), C_p is the specific heat at constant pressure of the gas mixture, and can also be obtained from the 9-coefficient NASA polynomial representation:

$$C_p = \sum_{i=1}^{ns} \frac{\rho_i}{\rho} C_{pi}, \tag{23}$$

$$\frac{C_{pi}}{R_i} = a_{1i}T^{-2} + a_{2i}T^{-1} + a_{3i} + a_{4i}T + a_{5i}T^2 + a_{6i}T^3 + a_{7i}T^4. \tag{24}$$

3. Particle combustion model

The combustion rate of solid particles is much slower than that of homogeneous gaseous reactions, often by one or several orders of magnitude, because it is always limited by the slow diffusion rates of reactants and products in the adjacent zone of the burning particle as well as by some slow surface chemical reactions [3,4,8,13,14]. Therefore, in solid particle combustion modeling, the combustion process is always divided into two steps. First, some mass of the particle is transferred into the gas phase as a vapor with a finite regression rate (J_{pk}). Then, this amount of particle vapor is reacted with the oxidizing gaseous species via infinitely fast reactions ($\dot{\omega}_i$), completely or partially, depending on the available amount of oxidizing gas. That is, the combustion rate of the particle has been determined by J_{pk} in most previous particle combustion models.

To date, three main particle combustion models have been widely used in gas-particle detonation simulations: the diffusion-controlled combustion model [15,16], the kinetic-controlled combustion model [19–22], and the surface-kinetic-oxidation and diffusion hybrid combustion model [23–25]. Although these models are in Eulerian forms, the corresponding Lagrangian forms to be used under the current Eulerian-Lagrangian framework can be easily derived from the original Eulerian forms. No extra physical consideration needs to be introduced. In this paper, the surface-kinetic-oxidation and diffusion hybrid combustion model [23] is employed to model the combustion rate of solid particles.

For the combustion of fine metal particles, the dependence of the burning rate on pressure has been identified in many experiments (i.e., [9,17,18]), which predicts the kinetics combustion regime for fine particles. Therefore, a combination of the kinetics combustion regime for fine particles and the diffusion combustion regime for large particles, namely the surface-kinetic-oxidation and diffusion hybrid combustion model, was proposed by Zhang et al. [23]. Its corresponding Lagrangian form of the combustion rate can be expressed as

$$J_{pk} = \pi d_{pk}^2 \frac{\upsilon_p W_p}{\upsilon_{\mathrm{oxi}} W_{\mathrm{oxi}}} k_{\mathrm{oxi}}, \tag{25}$$

with the mass depletion rate of the oxidizing gas k_{oxi}, caused by the combustion of the kth particle, expressed as

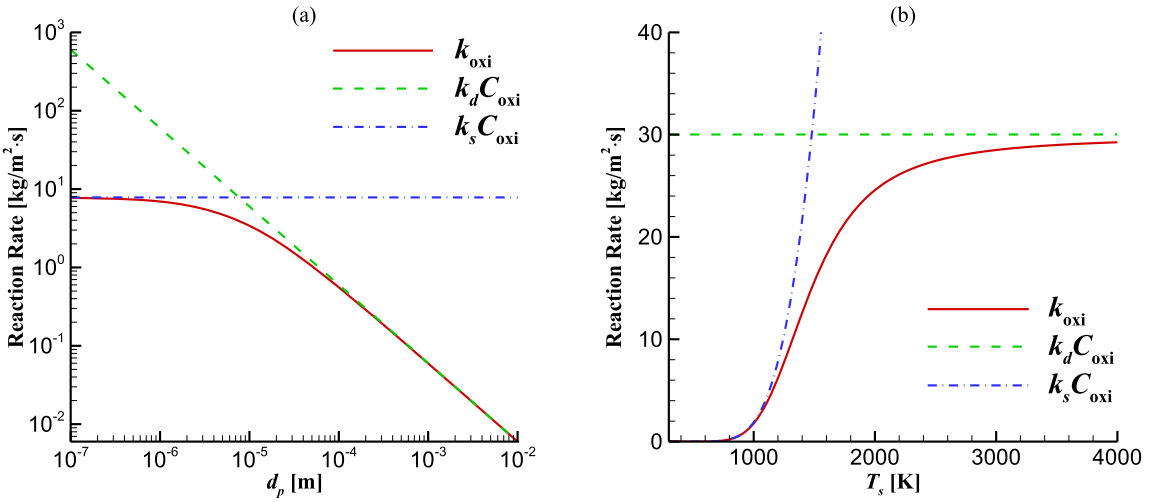

Fig. 1. Reaction rates of (a) different particle diameters at $T_s = 1200$ K and (b) different temperature at $d_p = 2$ μm.

$$k_{\text{oxi}} = \frac{k_{dk} k_{sk}}{k_{dk} + k_{sk}} C_{\text{oxi}}. \tag{26}$$

Here, k_{dk} and k_{sk} are the reaction rates for the diffusion combustion regime and the kinetics combustion regime, respectively, and C_{oxi} is the molar concentrations of oxidizing gas. k_{dk} and k_{sk} can be formulated as follows:

$$k_{dk} = \frac{\nu_{\text{oxi}} W_{\text{oxi}}}{\nu_p W_p} \frac{\rho_p d_{pk}}{2 C_{\text{total}} K d_{pk,0}^2} \left(1 + 0.276 \text{Re}_{pk}^{1/2} \text{Pr}^{1/3}\right), \tag{27}$$

and

$$k_{sk} = k_0 e^{-E_a / R_0 T_{sk}}. \tag{28}$$

In Eq. (29), W_p and W_{oxi} denote the molecular weights, and ν_p and ν_{oxi} denote the stoichiometric coefficients of particles and oxidizing gas, respectively; ρ_p is the particle material density; C_{total} represents the molar concentrations of the overall gas mixture; K is the diffusion reaction rate constant; and $d_{pk,0}$ is the initial diameter of the kth particle. In Eq. (28), $T_{sk} = (T + T_{pk})/2$ is assumed to be the particle surface temperature; k_0 and E_a are the reaction rate constant and the activation energy for the kinetics reaction regime, respectively.

Fig. 1 shows comparisons among the diffusion, kinetics, and the resulting hybrid reaction rates from Eqs. (26)–(28) as functions of the particle diameter and temperature for an Al-air mixture, where $K = 4 \times 10^6$ s/m^2, $k_0 = 1.2 \times 10^3$ kg m/mol s, and $E_a = 71.1$ kJ/mol. It can be seen that, the diffusion rate increases as the particle diameter reduces, but does not change with temperature. On the contrary, the kinetics rate is independent of the particle diameter but increases exponentially with temperature. Therefore, when the particle diameter is small (from Fig. 1(a)) or the temperature is low (from Fig. 1(b)), $k_s/k_d \ll 1$ and the hybrid combustion model would be reduced to the kinetics limit ($k_{\text{oxi}} \to k_s C_{\text{oxi}}$, Eq. (28)). On the other hand, when the particle diameter is large (from Fig. 1(a)) or the temperature is high (from Fig. 1(b)), $k_s/k_d \gg 1$ and the hybrid combustion model would be reduced to the diffusion limit ($k_{\text{oxi}} \to k_d C_{\text{oxi}}$, Eq. (28)). It is obvious that the above kinetics-diffusion hybrid combustion model is dependent on the particle size (inherent in the diffusion process), temperature (inherent in the kinetics combustion rate) and pressure (via oxidizing gas concentration). In the meanwhile, this hybrid model does not require an artificial particle ignition temperature, which is thought to be more capable of capturing the true combustion processes of reactive particles [24,25].

4. Numerical algorithm

4.1. In-house CE/SE scheme based on quadrilateral meshes

Since the introduction of the original CE/SE scheme by Chang and co-workers [32] in 1991, many types of CE/SE schemes have been developed based on different definitions of conservation elements (CEs) and solution elements (SEs). In this study, our in-house CE/SE scheme based on general quadrilateral meshes [50,51] is used to solve the conservation laws of gas-phase equations and to obtain the Eulerian-Lagrangian solutions of the two-dimensional gas-particle detonation problems. Fig. 2 depicts the space-time geometrical configuration of the quadrilateral-mesh-based two-dimensional CE/SE scheme. The projection of mesh points on the x–y plane is shown in Fig. 2(a), in which the interval between the staggered mesh points ● and ○ is $\Delta t/2$ in the time direction. The conservation element CE(P') is defined by the hexahedron $ACEGA'C'E'G'$ in

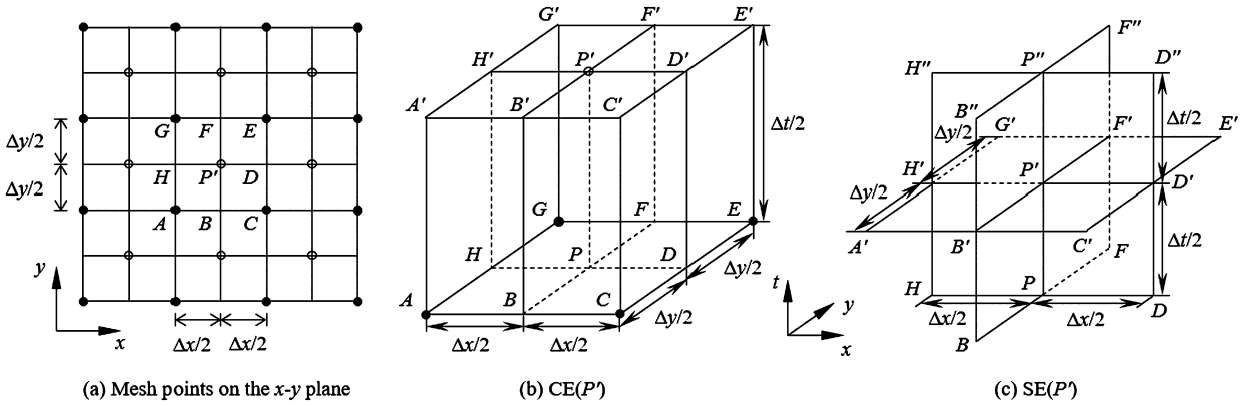

(a) Mesh points on the x-y plane (b) CE(P') (c) SE(P')

Fig. 2. Space-time geometrical configuration of the quadrilateral-mesh-based two-dimensional CE/SE scheme.

Fig. 2(b), and the solution element SE(P') is constituted by three orthogonal planes ($BFF''B''$, $DHH''D''$ and $A'C'E'G'$) intersecting at P' as demonstrated in Fig. 2(c). Based on the above definitions of CE and SE, the quadrilateral-mesh-based CE/SE scheme can be easily constructed and extended to the three-dimensional scenario directly.

Because the operator-splitting technique [53] is applied to treat the source terms of the gas-phase equations, the source terms in Eq. (1) are not considered at this stage. The treatment of the source terms in Eq. (1) will be addressed later in Section 4.2. When not considering source terms **S** and **W**, Eq. (1) can be rewritten as

$$\frac{\partial \mathbf{U}}{\partial t} + \frac{\partial \mathbf{F}}{\partial x} + \frac{\partial \mathbf{G}}{\partial y} = 0. \tag{29}$$

Let $x_1 = x, x_2 = y$ and $x_3 = t$ be the coordinates of a three-dimensional Euclidean space E_3. Then, Eq. (29) can be expressed as

$$\nabla \cdot \mathbf{H} = 0, \tag{30}$$

with the space-time flux vector $\mathbf{H} = (\mathbf{F}, \mathbf{G}, \mathbf{U})$. The conventional integral form of Eq. (29) can be given by

$$\int_V \nabla \cdot \mathbf{H} = 0, \tag{31}$$

where V is an arbitrary space-time domain in E_3.

By applying Gauss's divergence theorem, Eq. (31) can be rewritten as

$$\oint_{S(V)} \mathbf{H} \cdot d\mathbf{s} = 0, \tag{32}$$

where $S(V)$ is the boundary of the region V; $d\mathbf{s} = d\sigma \cdot \mathbf{n}$ with $d\sigma$ and $\mathbf{n}$ being the area and the unit outward normal vector of a surface element on $S(V)$, respectively.

Assume that the above integral conservation law, Eq. (32), is satisfied in the conservation element CE(P'); that is, let region V be CE(P'). Then, the integration in Eq. (32) can be expressed as follows:

$$\oint_{\mathrm{CE}(P')} \mathbf{H} \cdot d\mathbf{s} = \iint_{A'C'E'G'} \mathbf{U} dxdy - \iint_{ACEG} \mathbf{U} dxdy + \iint_{CEE'C'} \mathbf{F} dydt - \iint_{AGG'A'} \mathbf{F} dydt + \iint_{EGG'E'} \mathbf{G} dxdt - \iint_{ACC'A'} \mathbf{G} dxdt = 0. \tag{33}$$

To evaluate the integrations in Eq. (33), the physical variables at an arbitrary point $(x_{P'} + dx,\ y_{P'} + dy,\ t_{P'} + dt)$ in SE(P') can be approximated by the first-order Taylor's expansions at P':

$$\begin{cases} \mathbf{U}(dx, dy, dt)_{P'} = \mathbf{U}_{P'} + (\mathbf{U}_x)_{P'} dx + (\mathbf{U}_y)_{P'} dy + (\mathbf{U}_t)_{P'} dt, \\ \mathbf{F}(dx, dy, dt)_{P'} = \mathbf{F}_{P'} + (\mathbf{F}_x)_{P'} dx + (\mathbf{F}_y)_{P'} dy + (\mathbf{F}_t)_{P'} dt, \\ \mathbf{G}(dx, dy, dt)_{P'} = \mathbf{G}_{P'} + (\mathbf{G}_x)_{P'} dx + (\mathbf{G}_y)_{P'} dy + (\mathbf{G}_t)_{P'} dt, \end{cases} \tag{34}$$

where $\mathbf{X}_{P'}$, $(\mathbf{X}_x)_{P'}$, $(\mathbf{X}_y)_{P'}$ and $(\mathbf{X}_t)_{P'}$ are the values of $\mathbf{X}$ and its first-order derivatives respective to x, y and t at point P', respectively; and $\mathbf{X}$ represents **U**, **F** or **G**. Similarly, the same expansions can be applied to the other four SEs related to CE(P'), i.e., SE(A), SE(C), SE(E) and SE(G).

Accordingly, with Taylor's expansions to the first order in the five SEs related to CE(P'), Eq. (33) can be summarized as

$$\mathbf{U}_{P'} = \frac{1}{4}\left(\bar{\mathbf{U}} + \frac{\Delta t}{\Delta x}\bar{\mathbf{F}} + \frac{\Delta t}{\Delta y}\bar{\mathbf{G}}\right), \tag{35}$$

with

$$\begin{cases} \bar{\mathbf{U}} = \mathbf{U}\left(\frac{\Delta x}{4}, \frac{\Delta y}{4}, 0\right)_A + \mathbf{U}\left(-\frac{\Delta x}{4}, \frac{\Delta y}{4}, 0\right)_C + \mathbf{U}\left(-\frac{\Delta x}{4}, -\frac{\Delta y}{4}, 0\right)_E + \mathbf{U}\left(\frac{\Delta x}{4}, -\frac{\Delta y}{4}, 0\right)_G, \\ \bar{\mathbf{F}} = \mathbf{F}\left(0, \frac{\Delta y}{4}, \frac{\Delta t}{4}\right)_A - \mathbf{F}\left(0, \frac{\Delta y}{4}, \frac{\Delta t}{4}\right)_C - \mathbf{F}\left(0, -\frac{\Delta y}{4}, \frac{\Delta t}{4}\right)_E + \mathbf{F}\left(0, -\frac{\Delta y}{4}, \frac{\Delta t}{4}\right)_G, \\ \bar{\mathbf{G}} = \mathbf{G}\left(\frac{\Delta x}{4}, 0, \frac{\Delta t}{4}\right)_A + \mathbf{G}\left(-\frac{\Delta x}{4}, 0, \frac{\Delta t}{4}\right)_C - \mathbf{G}\left(-\frac{\Delta x}{4}, 0, \frac{\Delta t}{4}\right)_E - \mathbf{G}\left(\frac{\Delta x}{4}, 0, \frac{\Delta t}{4}\right)_G. \end{cases} \tag{36}$$

Equations (35) and (36) construct the unknown conserved-variable vector $\mathbf{U}$ at point P' at $t_A + \Delta t/2$ from the known vectors $\mathbf{U}$, $\mathbf{F}$, $\mathbf{G}$ and their derivatives respective to x, y and t at point A, C, E and G at t_A. Obviously, in order to evaluate the unknown variables at $t_A + \Delta t$, apart from the conserved-variable vector $\mathbf{U}$ at $t_A + \Delta t/2$, other vectors $\mathbf{F}$, $\mathbf{G}$ and their derivatives at $t_A + \Delta t/2$ must be known as well. Fortunately, as vectors $\mathbf{F}$ and $\mathbf{G}$ are functions of $\mathbf{U}$, the vectors required to be evaluated in the computation are $\mathbf{U}$, $\mathbf{U}_x$, $\mathbf{U}_y$ and $\mathbf{U}_t$. In addition, when substituting Eq. (34) into Eq. (29), one can obtain

$$(\mathbf{U}_t)_{P'} = -(\mathbf{F}_x)_{P'} - (\mathbf{F}_y)_{P'}. \tag{37}$$

Consequently, the final vectors needed to be evaluated at every half time step by the iterations are $\mathbf{U}$, $\mathbf{U}_x$ and $\mathbf{U}_y$.

The evaluation of derivatives of $\mathbf{U}$ respective to x and y at point P' can be obtained by using the continuous conditions at points A', C', E' and G':

$$\begin{cases} (\mathbf{U}_x)_{P'} = W\left[(\mathbf{U}_x)^-_{P'}, (\mathbf{U}_x)^+_{P'}, \alpha\right], \\ (\mathbf{U}_y)_{P'} = W\left[(\mathbf{U}_y)^-_{P'}, (\mathbf{U}_y)^+_{P'}, \alpha\right], \end{cases} \tag{38}$$

where

$$\begin{cases} (\mathbf{U}_x)^-_{P'} = -\frac{1}{\Delta x}\left[\mathbf{U}\left(0, 0, \frac{\Delta t}{2}\right)_A + \mathbf{U}\left(0, 0, \frac{\Delta t}{2}\right)_G - 2\mathbf{U}_{P'}\right], \\ (\mathbf{U}_x)^+_{P'} = +\frac{1}{\Delta x}\left[\mathbf{U}\left(0, 0, \frac{\Delta t}{2}\right)_C + \mathbf{U}\left(0, 0, \frac{\Delta t}{2}\right)_E - 2\mathbf{U}_{P'}\right], \\ (\mathbf{U}_y)^-_{P'} = -\frac{1}{\Delta y}\left[\mathbf{U}\left(0, 0, \frac{\Delta t}{2}\right)_A + \mathbf{U}\left(0, 0, \frac{\Delta t}{2}\right)_C - 2\mathbf{U}_{P'}\right], \\ (\mathbf{U}_y)^+_{P'} = +\frac{1}{\Delta y}\left[\mathbf{U}\left(0, 0, \frac{\Delta t}{2}\right)_E + \mathbf{U}\left(0, 0, \frac{\Delta t}{2}\right)_G - 2\mathbf{U}_{P'}\right]. \end{cases} \tag{39}$$

The weighted average function W in Eq. (38) is used to avoid numerical oscillations when dealing with discontinuities that are common in detonation problems, and it is defined as

$$W\left[x^-, x^+, \alpha\right] = \frac{|x^+|^\alpha x^- + |x^-|^\alpha x^+}{|x^+|^\alpha + |x^-|^\alpha}, \tag{40}$$

where α is an adjustable constant and usually equals 1–2.

4.2. Integration of source terms and particle Lagrangian equations

Source terms of the governing equations can be computed together with the space-time integration in the CE/SE scheme [35,41,42,51,54]. However, because the Jacobian matrixes of the source terms of interphase interactions and chemical reactions, which are required in the coupling treatment of source terms in the CE/SE scheme, are rather complicated to compute for two-phase detonation problems, especially under the Eulerian-Lagrangian framework, a separated treatment of these source terms is employed in this study. Notably, the good accuracy and stability of the CE/SE scheme have been proved preserved in high-speed reactive flow simulations [43,48,55], when source terms are treated separately. On the other hand, since the characteristic time scales of the source terms involving interphase interactions and chemical reactions are much smaller than that of flow dynamics, stiffness problems always occur in two-phase detonation simulations. Therefore, under the Eulerian-Lagrangian framework in this study, the source terms of interphase interactions and chemical reactions are explicitly integrated as ordinary differential equations (along with the integration of particle Lagrangian equations) by

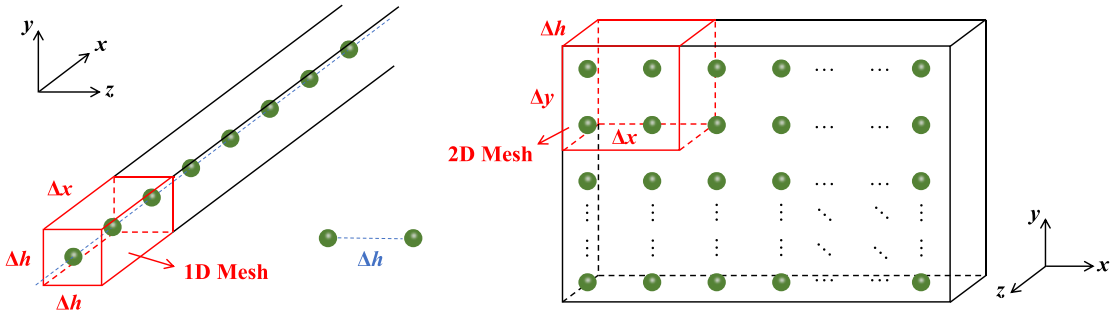

(a) One string of particles in 1D simulation **(b) One layer of particles in 2D simulation**

Fig. 3. Deployment of particles and equivalent 3D computational zones (● refers to a particle).

using an operator-splitting technique with multiple sub-time steps [53] to overcome the stiffness problems of two-phase detonation simulations. The detailed implementation process can be illustrated as follows:

$$\mathbf{U}_n \xrightarrow[\mathbf{S}=\mathbf{W}=0]{\text{Eq. (1)}} \widetilde{\mathbf{U}}_{n+1} \quad \Rightarrow \quad \begin{cases} \Delta t' = \Delta t/\mathrm{N} \\ \mathbf{U}_{n+1}^{(0)} = \widetilde{\mathbf{U}}_{n+1} \\ \mathbf{L}_{pk,n+1}^{(0)} = \mathbf{L}_{pk,n} \end{cases} \quad \Rightarrow \quad \begin{cases} \mathbf{U}_{n+1}^{(m)}, \mathbf{L}_{pk,n+1}^{(m)} \rightarrow \mathbf{S}^{(m)}, \mathbf{W}^{(m)}, \mathbf{S}_{pk}^{(m)} \\ \mathbf{U}_{n+1}^{(m+1)} = \mathbf{U}_{n+1}^{(m)} + \Delta t' \left[\mathbf{S}^{(m)} + \mathbf{W}^{(m)}\right] \\ \mathbf{L}_{pk,n+1}^{(m+1)} = \mathbf{L}_{pk,n+1}^{(m)} + \Delta t' \cdot \mathbf{S}_{pk}^{(m)} \end{cases}$$

$$\Rightarrow \quad \begin{cases} \mathbf{U}_{n+1} = \mathbf{U}_{n+1}^{(\mathrm{N})} \\ \mathbf{L}_{pk,n+1} = \mathbf{L}_{pk,n+1}^{(\mathrm{N})} \end{cases}, \tag{41}$$

where the subscripts n and m refer to the global time step (Δt) and the sub-time step ($\Delta t'$), respectively, and N is the total number of sub-time steps within one global convection time step of gaseous Euler equations. N can be chosen to be 10–20, depending on the degree of stiffness in the problem.

4.3. Deployment of particles

When tracking every particle individually under the Lagrangian framework, it is the specified number of particles that should be dealt with rather than the particle number density as in the two-fluid model of two-phase flows. To correctly evaluate the gas-particle interaction source terms in Eq. (5), the proper dV (the volume of the equivalent 3D computational mesh) needs to be chosen. Therefore, the gas-particle two-phase flow described under the Eulerian-Lagrangian framework is inherently a 3D problem. Assume that particles are space-uniformly dispersed in the physical 3D space with the same interparticle distance Δh in the x-, y- and z-directions initially. Taking the Al-air mixture with a particle diameter of 2 μm and density of 1.25 kg/m^3 as an example, the corresponding particle number density is roughly 1.1×10^{14}/m^3, yielding a mean interparticle distance of $\Delta h = 20.84$ μm. The computational cost for a 3D problem is extremely large, and 1D and 2D simulations are always carried out to investigate the gas-particle detonation problems under the assumption of initially uniform distribution of particles.

In 1D simulations, uniformities in the y- and z-directions are assumed and only the flow along the x-direction is calculated. Hence, only one string of particles is considered, along with the cross-section of the equivalent 3D computational zone (y–z plane) setting as $\Delta h \times \Delta h$, as shown in Fig. 3(a). Then, $dV = \Delta x \times \Delta h \times \Delta h$, where Δx is the 1D mesh size, and several particles are included within dV depending on the chosen size of Δx.

Similarly, uniformity in the z-direction is assumed in 2D simulations and the flow is developed along the x–y plane. Then, only one layer of particles in the equivalent 3D computational zone needs to be considered, along with the thickness (Δz) setting as Δh, as shown in Fig. 3(b). Therefore, $dV = \Delta x \times \Delta y \times \Delta h$, where Δx and Δy are the 2D mesh sizes. Again, the number of particles included within dV is dependent on the chosen sizes of Δx and Δy.

5. Parallel technology

5.1. MPI communication cost in Eulerian-Lagrangian framework

The emphasis on the parallel implement technology in this paper is due to the formidable communication costs when MPI parallelization is applied to the Eulerian-Lagrangian framework to solve the high-speed gas-particle flows by using the traditional data structures. It is well known that in single-phase fluid dynamics, the flow field is generally represented and solved in the Eulerian coordinate. Therefore, static arrays are often used to store flow field information in computer codes, mainly due to the simplicity in implementation and convenience of addressing, especially when structured grids are

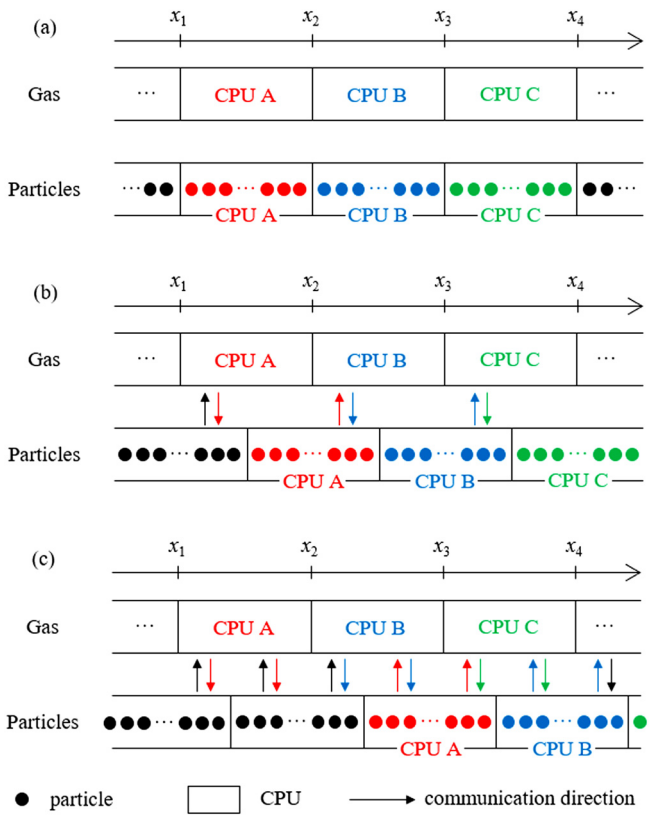

Fig. 4. Static array structure under the Eulerian-Lagrangian framework. (For interpretation of the colors in the figure(s), the reader is referred to the web version of this article.)

employed. The popular use of static arrays also stems from two historical reasons: first, in early CFD codes, the application of arrays makes codes written in Fortran be of high efficiencies; second, when MPI parallelization technology is introduced to accelerate the solution of problem, the convenience of static array is preserved, and only the boundary information of the computational zone for each CPU is needed to communicate with other adjacent CPUs, leading to the great success of the combination of MPI and static arrays in single-phase flow solutions.

However, when the Eulerian-Lagrangian framework is employed to solve high-speed gas-particle two-phase flows, the use of MPI parallelization technology with static arrays is of great difficulties. In the Eulerian-Lagrangian framework, the Eulerian framework is still used to represent and solve the gas-phase flow, while the Lagrangian framework is used to represent and solve the motion of particles. Apparently, the use of static arrays in the Eulerian framework is not problematic, but obstacles arise when storing particle information in static arrays. Taking the 1D two-phase flow interacted with a string of particles as an example (Fig. 4), at the initial moment, information about gas and particles at the same location is stored in the same CPU (Fig. 4(a)). No communication between CPUs for calculating gas-particle interactions is needed, and only the boundary information of the computational zone of each CPU needs to be transferred. Notably, relative motion between the gas and particles is inherent in high-speed two-phase flows. Hence, as time proceeds, the information related to gas in the Eulerian framework and particles in the Lagrangian framework will be staggered, as shown in Fig. 4(b). At this time, when gas-particle interactions are calculated, information on the gas and particles must be transferred between CPUs. For example, when gas-particle interactions in the zone of $[x_2, x_3]$ are being calculated, apart from particle information (colored in blue) remaining in CPU B, particle information (colored in red) in CPU A should also be considered along with the gas information stored in CPU B. Therefore, a large amount of information between CPU B (about the gas) and CPU A (about the particles) should be transferred between each other. Besides, the scale of communication is determined by the number of particles stored in CPU A and meanwhile staggered with CPU B. As time proceeds further, information in the Lagrangian framework will be completely staggered with that in the Eulerian framework, as shown in Fig. 4(c). At this moment, when gas-particle interactions are calculated, information about all particles stored in CPU A should be transferred to other CPUs (CPU B and CPU C), and information about the gas stored in other CPUs should be transferred to CPU A as well. If the number of particles stored in each CPU is N in the initial state, then the cost of communication for calculating gas-particle interactions will be of the magnitude of $O(N)$. It should be noted that, N is a huge number in most gas-particle flows, and it is always larger than the number of meshes of the gas phase in each CPU. That is, the cost of communication may be even larger than the cost of computation. Therefore, when comparing with the cost of computation or the amount of information

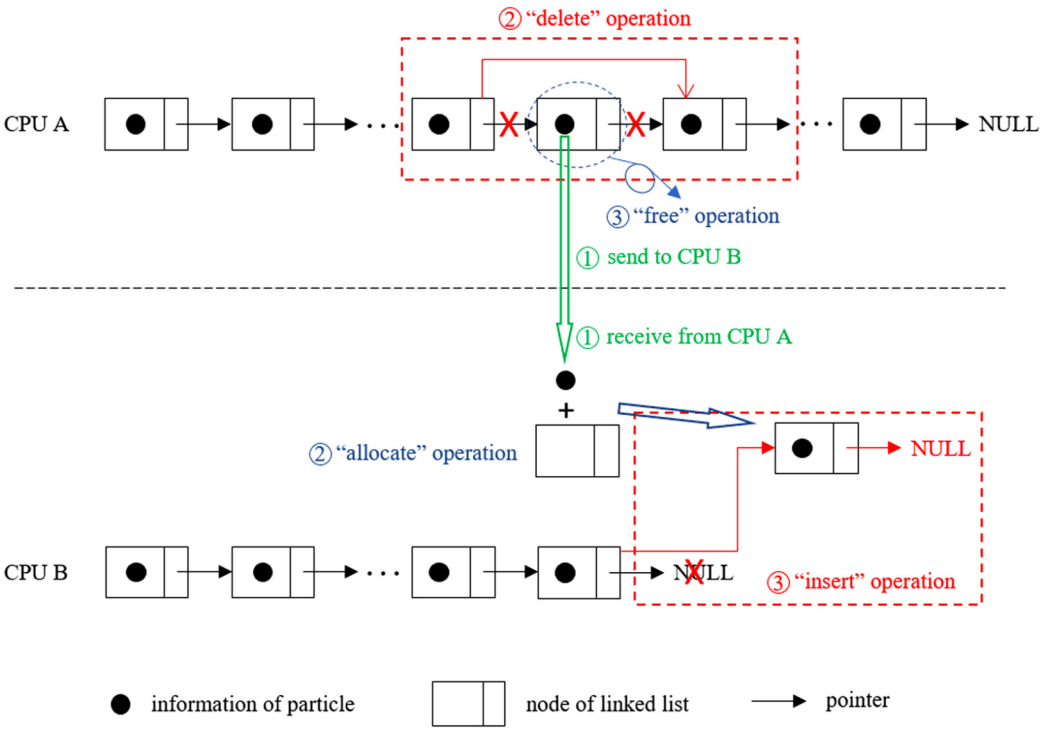

Fig. 5. Linked lists and operation sequence.

needed to be transferred to other CPUs in single-phase flows (only boundary information of the computational zone for each CPU), the amount of information transfer about particles and gas between CPUs is dreadful in these gas-particle flows when using static arrays to store particle information.

5.2. MPI implement using new data structure

The communication problem of MPI parallelization under the Eulerian-Lagrangian framework and the inherent disadvantage of using static arrays to store particle information have been demonstrated in detail in the previous section. Notably, the order in which particles are presented in the Lagrangian framework is not as necessary as that for the gas phase in the Eulerian framework; that is, one does not need to store the initial location relationship among particles. The only operation required for coding is to traverse every particle one by one. Therefore, a new dynamic data structure, namely the linked list, is introduced to store particle information and solve the communication problem in this work.

As shown in Fig. 5, each CPU owns one linked list to store information of the particles that are at the corresponding locations to the gas phase. In each linked list, one node represents one particle and consists of two parts: the data part that stores particle information, and the pointer that points to the next node of the particle. The pointer of the last node of the linked list points to the "NULL", which means that the list has ended. This kind of linked list is a common dynamic data structure in advanced programming and works well in the MPI parallelization of gas-particle two-phase flow solutions, as will be discussed later in Section 5.3.

In addition, four basic operations of the linked list are needed as well: allocate, free, delete and insert. The "allocate" operation is used to allocate new memory to store information about the "new" particle, the "free" operation to free the memory that stores information about an "old" particle, the "delete" operation to remove one particle from the linked list, and the "insert" operation to add one particle at the end of the linked list, as depicted in Fig. 5.

The whole operation sequence about the above-mentioned four basic operations is explained as follows. When the particle phase is staggered with the gas phase because of relative motion, the information of the particles, whose locations exceed the corresponding location ranges assigned to the present CPUs, will be transferred to and stored in the CPUs with the correct particle location ranges. For CPU A in Fig. 5, where one particle is removed,

1. send the information of the specific particle to CPU B;
2. delete the particle node from the linked list;
3. free the memory of the separated node.

Meanwhile, for CPU B in Fig. 5, where a new particle is received, the corresponding operation sequence is

1. receive the information of the new particle from CPU A;
2. allocate a new node and store the information into the data field of the node;
3. insert the new particle node at the end of the linked list.

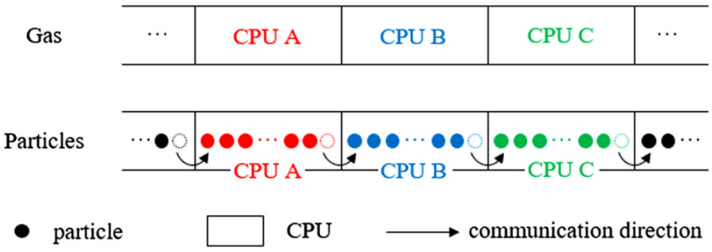

Fig. 6. Dynamic data structure using the linked list in Eulerian-Lagrangian framework list.

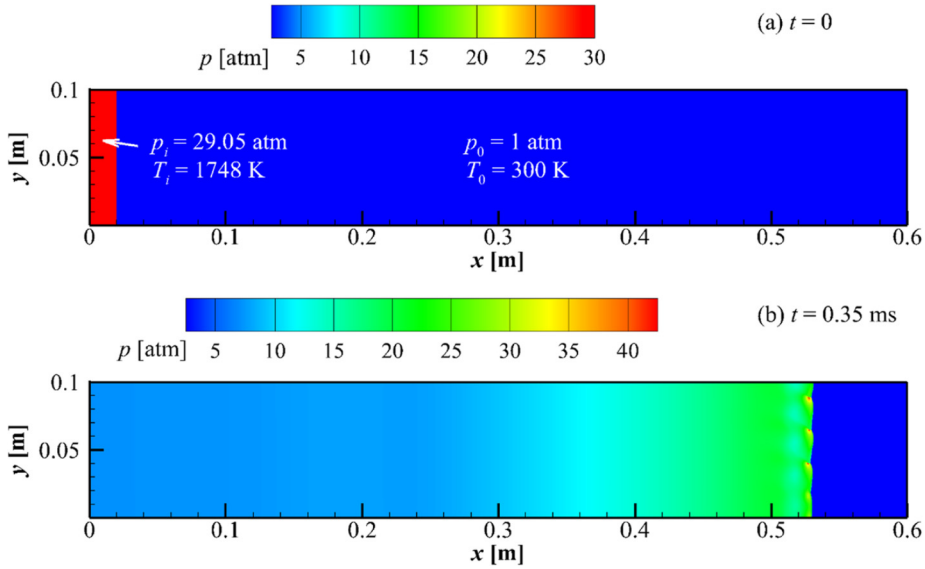

Fig. 7. MPI parallel test of a 2D Al-air detonation propagation problem.

With this dynamic data structure and the corresponding operation sequences, information about Lagrangian particles is always stored in the CPUs of the correct Eulerian coordinates, and therefore excessive communication between CPUs when calculating gas-particle interactions is avoided, as shown in Fig. 6. Moreover, with the limitation of the CFL condition, only "one" particle at most will cross the CPU boundary at every iteration; that is, the information of "one" particle at most will be transferred to the other CPU at one iteration step by the above operation sequence. As a result, the communication cost of the MPI parallel for the gas-particle interaction calculation will be reduced from O(N) to O(1) when using this data structure. Furthermore, with the limitation of the CFL condition, the physical location of a Lagrangian particle only moves to the adjacent gas-phase Eulerian mesh within one timestep; that is, when a particle moves to another CPU, the target CPU must be the adjacent one. Therefore, the target CPU can be easily tracked by using a CPU map stored in a static array and the cost for tracking the adjacent CPU can be neglected, compared with those spent on flow field solutions and MPI data communications.

5.3. Parallel performance

To demonstrate the MPI parallelization performance with the use of linked lists, a 2D Al-air detonation propagation problem is tested in this section. The initial states of the flow field are $p_0 = 1$ atm and $T_0 = 300$ K, and a small ignition zone with high pressure and temperature is set at the left end of the domain, as shown in Fig. 7(a). The mesh size used is $\Delta x = \Delta y = 0.05$ mm, which results in approximately 24 million meshes in the computational domain (600 mm $\times$ 100 mm). The concentration of Al particles is $\Omega_p = 0.5$ kg/m^3, and the size of the Al particles is $d_p = 2$ μm, resulting in about 75 million particles in the computational domain.

All MPI parallel tests are carried out on the Tianhe-2 super computer from China with core numbers of 1, 2, 3, 4, 6, 12, 24, 48, 96, 192 and 384. The use of one core means that the calculation is done serially. Each computation node of Tianhe-2 consists of two 12-core Xeon E5 2692 processors with 64 GB RAM, and a high-speed interconnect technology, called TH Express-2, with a speed of 80-140 Gb/s is used in data communications between computation nodes. The typical result of the tested problem at $t = 0.35$ ms is shown in Fig. 7(b), with 384 cores. The parallel performance is evaluated by the speedup parameter, which is calculated by dividing the time used in parallel calculation using different cores with that in serial calculation, and the results are presented in Fig. 8 along with the ideal speedups. Notably, the MPI parallelization by

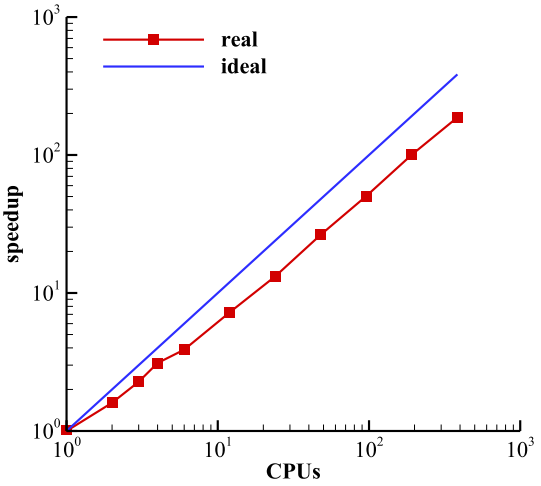

Fig. 8. Speedups of the tested problem using linked lists.

using static arrays is impossible, even with only 2 cores, as the communication cost would be unacceptably large, which has been explained in Section 5.1. Therefore, the parallel efficiency by using static arrays would be obviously very low and is not given here. As indicated in Fig. 8, when 384 cores are used, the code using linked lists still has a reasonable parallel efficiency of about 50% for the tested problem, which means that the linked list data structure works well in the MPI implement when solving gas-particle two-phase flows.

6. Numerical examples

With the details of physical models and numerical technologies described in previous sections, a computer code for simulating gas-particle two-phase high-speed reactive flows has been developed under an Eulerian-Lagrangian framework using the CE/SE method with MPI parallelization. In this section, the developed computer code will be carefully validated by three traditional problems that were investigated under the Eulerian-Eulerian framework, including the 1D inert gas-particle shock tube problems [31] and the 1D and 2D gas-particle detonation problems with a hybrid combustion model [23,24]. In the end, in order to show the superiorities of the Eulerian-Lagrangian code in realistic gas-particle detonation simulations, polydisperse gas-particle detonations with log-normal particle size distributions, which are infeasible under the Eulerian-Eulerian framework, are investigated and compared with their monodisperse counterparts.

6.1. Gas-particle shock tube problems with no combustion

The high-speed gas-particle (dusty-gas) flows, especially the non-stationary ones, which are always characterized by non-equilibrium transition regions due to momentum and energy exchanges between the two phases, are very different from their pure gas counterparts [30]. In this section, the traditional 1D inert gas-particle shock tube problems, which have been investigated numerically by Saito et al. in [31], are simulated to test the capacities of the developed computer code in capturing the non-equilibrium two-phase transport processes in unsteady gas-monodisperse particle flows with no combustion.

The shock waves are propagating in the mixture consisting of fine inert glass particles ($\rho_p = 2500$ kg/m^3, $d_p = 10$ μm) suspended in air. Aside from treating the air as a calorically perfect gas with the ratio of specific heats of $\gamma = 1.4$, the problems are modeled as described in previous sections. In [31], the results were given in the non-dimensional forms, and the reference state parameters were chosen as the initial states in the driven section of the shock tube, namely $p_{\text{ref}} = 1.013 \times 10^5$ Pa, $\rho_{\text{ref}} = 1.293$ kg/m^3, $T_{\text{ref}} = 271.8$ K. Other reference quantities were given as below,

$$u_{\text{ref}} = \sqrt{\frac{p_{\text{ref}}}{\rho_{\text{ref}}}}, \qquad L_{\text{ref}} = \frac{4}{3}\frac{\rho_p}{\rho_{\text{ref}}} d_p, \qquad t_{\text{ref}} = \frac{L_{\text{ref}}}{u_{\text{ref}}}. \tag{42}$$

Two cases characterized by different propagation regimes of shock waves as described in [31] are simulated in this section and the chosen mesh sizes in both cases are $\Delta x / L_{\text{ref}} = 0.01$. Since the computation scales of these 1D cases are small, serial computations (with 1 core) are performed in this section and the simulation results are obtained within 1 hour.

The first case being simulated is the so-called partially dispersed one. The initial conditions of the problem are given in Eq. (43). In this case, the leading shock is propagating at a constant speed after a short transition period, and the steady frozen shock wave Mach number is about $\text{Ma}_f = 1.207$, as shown in Table 1. The Ma_f is greater than 1; that is, the shock

Table 1
Frozen and equilibrium shock Mach numbers for problems in Eqs. (43) and (44).

	Partially dispersed case, Eq. (43)		Completely dispersed case, Eq. (44)	
	Ma_f	Ma_e	Ma_f	Ma_e
Present	1.207	1.843	0.915	1.398
In Ref. [31]	1.2	1.8	0.9	1.4

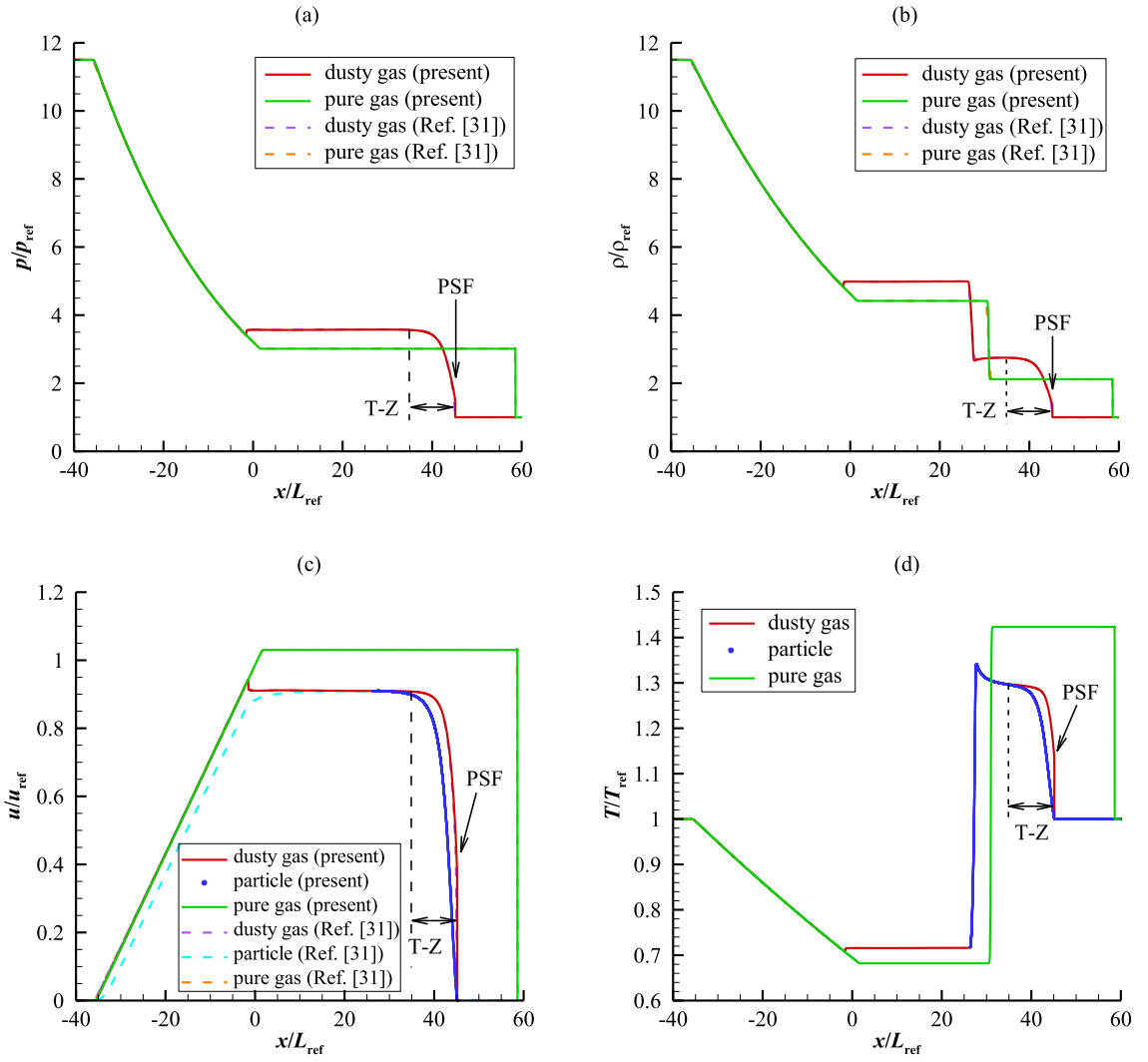

Fig. 9. Solutions of the gas-particle shock tube problem with initial conditions of Eq. (43) at $t/t_{\text{ref}} = 30$: (a) pressure, (b) density, (c) velocity and (d) temperature.

wave propagation mode is supersonic. Therefore, the shock wave will be characterized by a partially sharp front (PSF) followed by a transition zone (T-Z), which can be clearly seen in Fig. 9.

$$\left(\frac{\rho}{\rho_{\text{ref}}}, \frac{u}{u_{\text{ref}}}, \frac{p}{p_{\text{ref}}}, \frac{\Omega_p}{\rho_{\text{ref}}}, \frac{u_p}{u_{\text{ref}}}\right) = \begin{cases} (11.5, 0, 11.5, 0, 0), & x < 0, \\ (1, 0, 1, 1, 0), & x \geq 0. \end{cases} \tag{43}$$

Further, in the transition zone, significant lags between gas and particles in the changes of velocity and temperature can be observed in Figs. 9(c) and 9(d), implying non-equilibrium thermal and mechanical processes between gas and particles. In this case, the transition length, which is defined by a 99% ratio of u_p/u, is 10.2 L_{ref}.

Another case being simulated, as described by the initial conditions of Eq. (44), is the so-called completely dispersed dusty shock wave, which shows different shock wave characteristics with those of the partially dispersed shock. In this case, the shock wave is propagating in the subsonic mode, as the Ma_f is smaller than 1 ($Ma_f = 0.915$ as shown in Table 1).

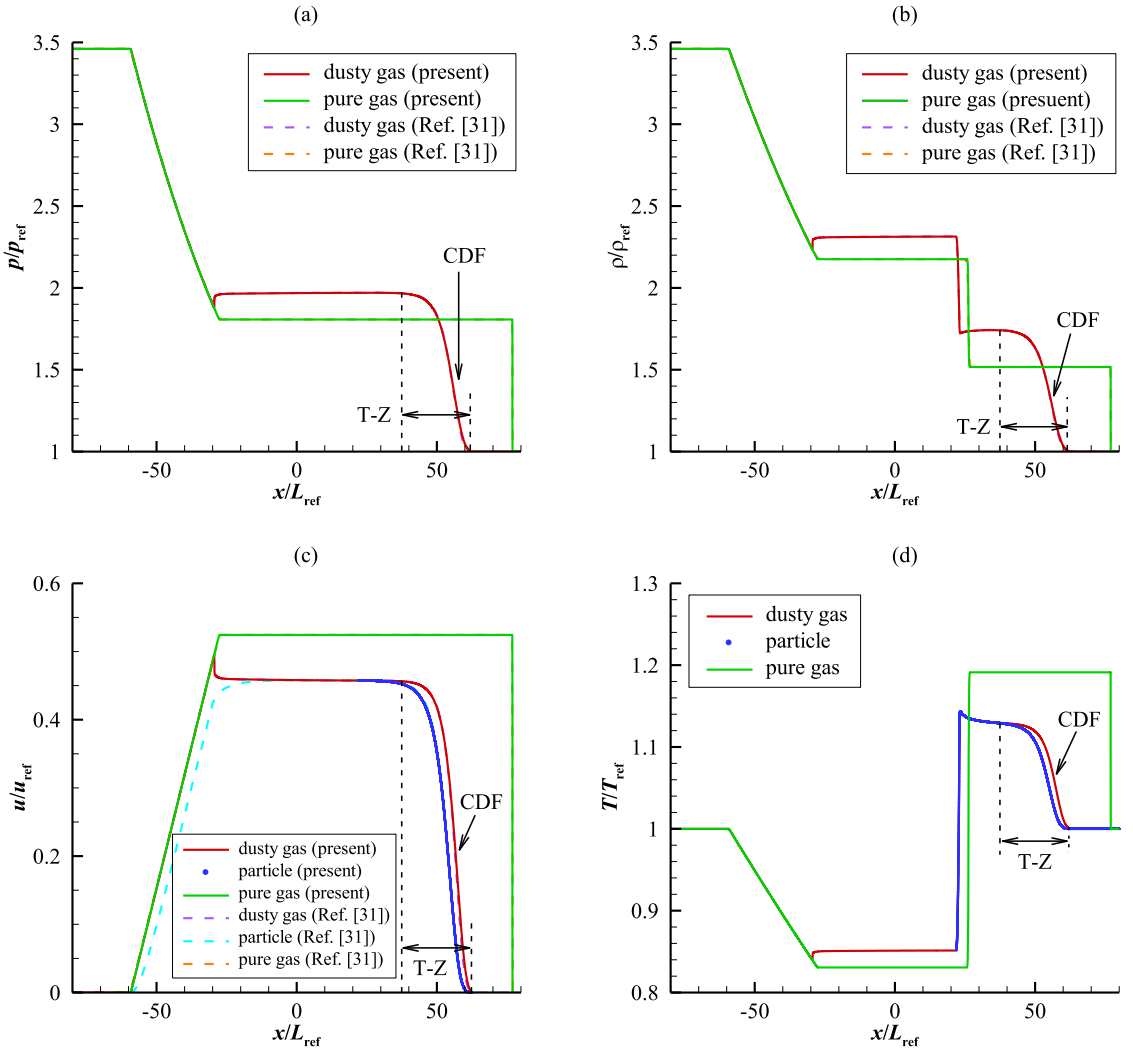

Fig. 10. Solutions of the gas-particle shock tube problem with initial conditions of Eq. (44) at $t/t_{\text{ref}} = 50$: (a) pressure, (b) density, (c) velocity and (d) temperature.

Therefore, the shock wave will be characterized by a completely dispersed front (CDF) interacted with the transition zone (T-Z), as indicated in Fig. 10. Nevertheless, the shock wave speed is still at a constant value, and the equilibrium shock wave Mach number is essentially greater than 1 ($\text{Ma}_e = 1.398$). Moreover, it can be revealed that, the transition length is 24.3 L_{ref} for this case, which is larger than that of the partially dispersed case. Hence, the effects of the momentum and energy exchanges between two phases on shock wave propagation are greater in the completely dispersed case.

$$\left(\frac{\rho}{\rho_{\text{ref}}}, \frac{u}{u_{\text{ref}}}, \frac{p}{p_{\text{ref}}}, \frac{\Omega_p}{\rho_{\text{ref}}}, \frac{u_p}{u_{\text{ref}}}\right) = \begin{cases} (3.46, 0, 3.46, 0, 0), & x < 0, \\ (1, 0, 1, 1, 0), & x \geq 0. \end{cases} \tag{44}$$

Moreover, the detailed results available in [31] of the above two cases have also been provided in Table 1 and Figs. 9–10 for comparisons. Obviously, the calculated shock Mach numbers agree well with those given in [31]. And all distributions of flow parameters obtained by the developed code in this paper overlap those in [31], except the differences in the particle profiles. As illustrated in Figs. 9(c), 9(d), 10(c) and 10(d), the spatial distributions of particles in this paper are terminated at the contact discontinues, whereas the curves in [31] are extended to the driver section of the tube. This is because the Eulerian-Eulerian simulations conducted in [31] could not deal with "zero" particle concentration in the driver section of the tube. The compromise treatment is to set the particle concentration at a very low value (such as 10^{-6} ρ_{ref}) at the location where it should be zero. However, this problem no longer exists in the Eulerian-Lagrangian simulations in this paper, since the "zero" particle concentration is simply achieved by setting no particle at that location.

From the results above, it can be concluded that depending on the frozen shock wave Mach number, there are two propagation regimes of shock waves in gas-particle mixtures, namely the partially and completely dispersed shock waves.

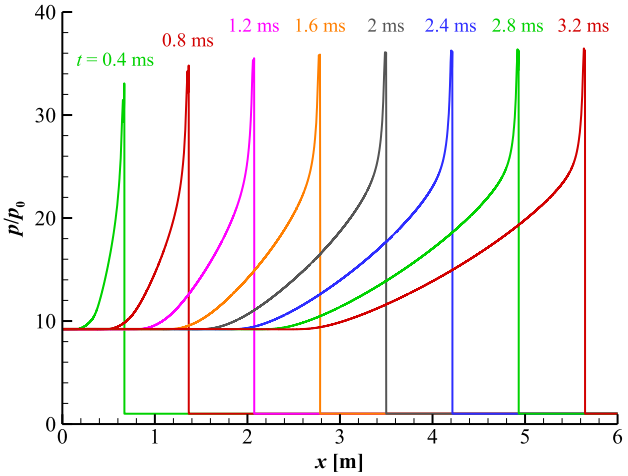

Fig. 11. Time evolutions of pressure distributions of the 2-μm Al-air detonation with constant heat capacities, at $t = 0.4, 0.8, \ldots, 3.2$ ms.

This conclusion is consistent with that obtained by the Eulerian-Eulerian simulations of Saito et al. in [31], which reveals the good capacity of the developed Eulerian-Lagrangian CE/SE code in inert high-speed gas-monodisperse particle flow simulations.

6.2. 1D gas-particle detonation using hybrid combustion model

The surface-kinetic-oxidation and diffusion hybrid combustion model, as described in Section 3, was firstly proposed by Zhang et al. [23]. In the same work, Zhang et al. applied this hybrid combustion model in their Eulerian-Eulerian simulations of Al-air two-phase detonations [23]. Herein, the same case of Zhang et al. [23] is simulated by our developed Eulerian-Lagrangian code with implementation of the hybrid combustion model for validation of the code.

The detonation wave is propagating in the dilute mixture consisting of small spherical Al particles suspended in air. The air is initially at an elevated pressure of $p_0 = 2.5$ atm and a temperature of $T_0 = 300$ K. The concentration of Al particles is $\Omega_p = 1.25$ kg/m^3, and the particle diameter is $d_p = 2$ μm. For Al particles, the parameters in the hybrid combustion model, Eqs. (25)–(28), are given by $K = 4 \times 10^6$ s/m^2, $k_0 = 1200$ kg m/(mol s), and $E_a = 71.1$ kJ/mol. Following the approach of Zhang et al. [23] and the experimental observations of single Al particle combustion in Olsen and Beckstead [56], the assumptions are made that the oxidation of Al takes place on the particle surface and the product Al_2O_3 exists in the form of condensed state along with the condensed Al, rather than in the gas phase. That is, a particle, when burning, is assumed to be composed of two parts: Al and Al_2O_3. Accordingly, the combustion of Al particles is expressed by the following single-step global chemical reaction with a heat of reaction of 838 kJ/mol:

$$\mathrm{Al} + \frac{3}{4}\mathrm{O_2} \rightarrow \frac{1}{2}\mathrm{Al_2O_3}, \quad \Delta H_m = -838 \text{ kJ/mol}. \tag{45}$$

No decomposition and evaporation of the product Al_2O_3 is considered [23]. Meanwhile, the melting and evaporation points of Al in [23] are set at 933.6 K and 2465 K, respectively; and the latent heats of Al melting and evaporation processes are 10.7 and 290 kJ/mol, respectively. The melting point of Al_2O_3 is given at 2327 K. The melting latent heat of Al_2O_3 is neglected in these simulations due to its rather small magnitude. The internal energies of the particle components in [23] are evaluated via constant heat capacity values of 24.2 J/(mol K) for Al and 79.3 J/(mol K) for Al_2O_3.

Based on the above details of the hybrid combustion model of Al particles, 1D simulation results of the same Al-air two-phase detonation as in [23] are obtained by the developed Eulerian-Lagrangian code in this paper, as shown in Figs. 11 and 12. The grid size used in the simulation is chosen to be $\Delta x = 0.2$ mm, which has been validated by careful convergence tests to exclude the influences of grid resolutions. Because large number of reactive Al particles (about 0.3 million) are under consideration in this 1D case, 24 cores (one node of the Tianhe-2 super computer) with MPI parallel are chosen to reduce the running time (∼12 hours) with a reasonable parallel efficiency.

Fig. 11 presents the time evolution of pressure distributions along the 1D computational zone from 1 to 3.2 ms with a time interval of 0.4 ms. It can be seen that the detonation wave forms after a short transition period and reaches its steady state after about 1.2 ms. The calculated 1D detonation speed is equal to $D = 1793$ m/s, and the peak pressure is equal to $p_{\max}/p_0 = 36.47$. In the simulations of Zhang et al. [23], the calculated 1D detonation speed is equal to $D = 1758$ m/s, and the peak pressure is equal to $p_{\max}/p_0 = 36.63$. Good agreement is observed.

The comparisons of pressure, gas temperature and particle temperature profiles at $t = 3.2$ ms with those in Zhang et al. [23] are illustrated in Fig. 12. As seen, all the profiles in present simulation agree well with those in previous simulations.

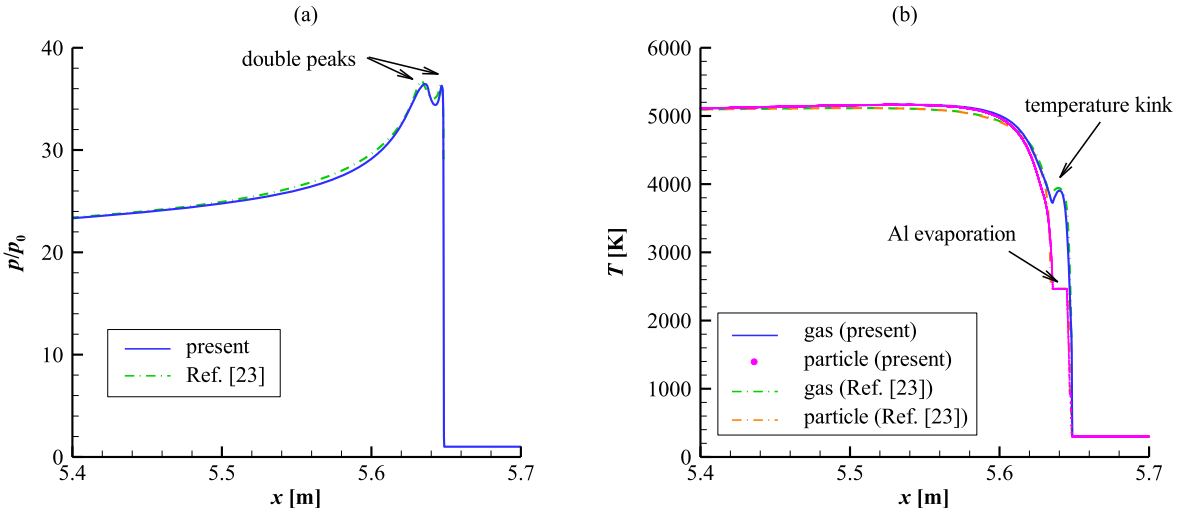

Fig. 12. Profiles in the 2-μm Al-air detonation front with constant heat capacities, at $t = 3.2$ ms, (a) gas pressure and density, (b) temperatures of gas and particles.

The maximum product temperature is about 5150 K in present simulation, while it is about 5100 K in previous simulations (Fig. 12(b)). The two-phase detonation characteristics with condensed combustion products, identified in previous Eulerian-Eulerian simulations [23], can be well captured in the present Eulerian-Lagrangian simulation, including the double pressure peaks shown in Fig. 12(a), and Al evaporation plateau and gas temperature kink shown in Fig. 12(b). Additionally, the non-equilibrium feature of thermal processes between gas and particles is also well delineated, as evidenced by the temperature lag between these two phases in Fig. 12(b).

Notably, constant heat capacities were used in the above simulations. Nevertheless, as discussed by Teng et al. [25], the use of constant heat capacities in the evaluation of internal energies of the condensed phases (Al and Al_2O_3) is not physics-consistent. When heat capacities of Al and Al_2O_3 are described as functions of temperature and introduced into this case using Eq. (9), the calculated 1D detonation speed and peak pressure are then equal to $D = 1535$ m/s and $p_{max}/p_0 = 27.25$, respectively. The corresponding values in the experiments of Zhang et al. [9] are $D = 1460$–1500 m/s and $p_{max}/p_0 = 26.0$–28.4, respectively. The simulation results using realistic heat capacities of Al and Al_2O_3 concur well with the experimental observations.

6.3. 2D detonation cell structure using hybrid combustion model

The hybrid combustion model by Zhang et al. [23] has been applied in the Eulerian-Eulerian simulations of Briand et al. [24] to model the detonation cellular structures of Al-gas suspensions as in experiments of Zhang et al. [8] and Ingignoli et al. [12]. In the experiments of Zhang et al. [8], the two-phase mixture consists of flake Al particles with an estimated equivalent diameter of $d_p = 13.5$ μm and air at standard pressure and temperature. The particle concentration is $\Omega_p = 0.5$ kg/m^3 and the measured detonation cell width is approximately $\lambda = 40$ cm. In the experiments of Ingignoli et al. [12], the two-phase mixture consists of flake Al particles with an estimated equivalent diameter of $d_p = 8.6$ μm and pure oxygen at standard pressure and temperature. The particle concentration is $\Omega_p = 1.5$ kg/m^3 and the measured detonation cell width is about $\lambda = 5$–10 cm.

Different from Zhang et al. [23], the product Al_2O_3 was still treated as a gas in the simulations of Briand et al. [24]. The parameters in the hybrid combustion model, Eqs. (25)–(28), are given by $K = 1.6 \times 10^6$ s/m^2, $E_a = 71.1$ kJ/mol, and $k_0 = 8.2 \times 10^3$ and 6.6×10^4 kg m/(mol s) for the Al-air detonation in Zhang et al. [8] and the Al–O_2 detonation in Ingignoli et al. [12], respectively. The results obtained by the developed Eulerian-Lagrangian code with 192-core MPI parallel (8 nodes of the Tianhe-2 super computer) are shown in Figs. 13 and 14. Notably, this core number is chosen to obtain simulation results within an acceptable running time (∼8 days) in these 2D cases. It can be revealed that both cellular structures in the Al-air and Al–O_2 detonations are regular in size. The simulated cell widths are about $\lambda = 40$ cm and $\lambda = 10$ cm for the Al-air detonation in Zhang et al. [8] and the Al–O_2 detonation in Ingignoli et al. [12], respectively, which agree well with their experimental observations. Meanwhile, the similar results have been obtained by Briand et al. [24].

6.4. Polydisperse gas-particle detonation

6.4.1. Log-normal particle size distribution

In reality, dust materials in industries and experiments are always characterized by a specific particle size distribution, with a relatively wide range of particle diameters [5,9,23]. That is, particle suspensions are always polydisperse in size,

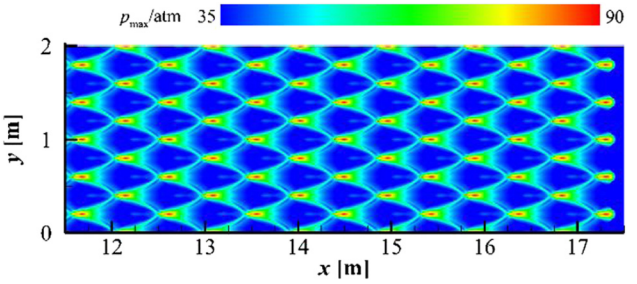

Fig. 13. Traces of maximum pressure in the Al-air detonation ($d_p = 13.5$ μm, $\Omega_p = 0.5$ kg/m^3) by the developed Eulerian-Lagrangian code.

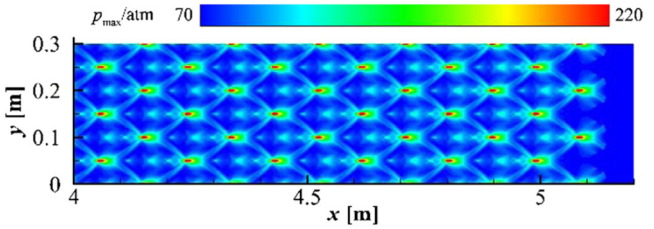

Fig. 14. Traces of maximum pressure in the Al–O_2 detonation ($d_p = 8.6$ μm, $\Omega_p = 1.5$ kg/m^3) by the developed Eulerian-Lagrangian code.

rather than monodisperse with only one particle size as discussed in the above sections and in most of previous studies. In non-equilibrium gas-particle flows, the forces acted upon and the heat transferred to particles from gases differ by the particle size. And in reactive particle flows, particle combustion rates also depend on the particle size [15,23]. As a result, many characteristics of gas-particle detonations are significantly influenced by the particle size, including initiation energy, deflagration-to-detonation transition (DDT) distance, burning time, length of reaction zone, cell size, etc. [8,22,26,27]. Therefore, it is important to systematically study the features of polydisperse gas-particle detonation, the differences with monodisperse detonation, and the effects of multiple time and length scales in a specific particle size distribution. However, the traditional Eulerian-Eulerian method has its own limitations in addressing these problems, because different temperatures, velocities and sizes of particles should be distinguished within one computational mesh. Contrarily, the Eulerian-Lagrangian method, which tracks every Lagrangian particle of the condensed phase by Newton's laws of motion, is capable of simulating polydisperse gas-particle detonation. Accordingly, in this section both 1D and 2D polydisperse Al-air detonations with log-normal particle size distributions are studied by the developed Eulerian-Lagrangian code, and the results are compared with those of monodisperse Al-air suspensions, to demonstrate the superiorities of the Eulerian-Lagrangian method in realistic gas-particle detonation simulations.

The log-normal particle size distribution, $f_n(d_p)$, frequently used to represent the sizes of solid particles [58], is firstly introduced as follows:

$$f_n(d_p) = \frac{1}{\sqrt{2\pi}\sigma_0} \exp\left[-\frac{1}{2}\left(\frac{\ln d_p - \ln d_{nM}}{\sigma_0}\right)^2\right]\frac{1}{d_p}, \tag{46}$$

where d_{nM} and σ_0 are the number median diameter and standard deviation of the distribution, respectively. Accordingly, in numerical simulations, the particles are uniformly distributed in the computation domain with the same particle number density as described in Section 4.3, and particle diameters are set by a random number generator using Eq. (46).

In the Al-air detonation experiment of Zhang et al. [9], which has been simulated in Section 6.2 as a monodisperse detonation, the test material is actually micrometric-grade atomized Al with a nominal diameter (volume-average diameter, $\bar{d}$) of 2 μm, known as H-2 Al, supplied by Valimet Incorporated. The detailed scanning electron micrograph of the test H-2 Al particles can be found in [9].

An important relationship for the calculation of various mean diameters of the log-normal distribution is

$$\int_0^\infty s^k f_n(s)ds = d_{nM}^k e^{\sigma_0^2 k^2/2}, \tag{47}$$

where s is the integration variable. As indicated in Zhang et al. [23], another parameter describing the test H-2 Al particles is the mass-weighted-average particle diameter $\bar{d}_m = 3.3$ μm. The $\bar{d}$ and $\bar{d}_m$ can be calculated by integrations of $f_n(d_p)$ with Eq. (47):

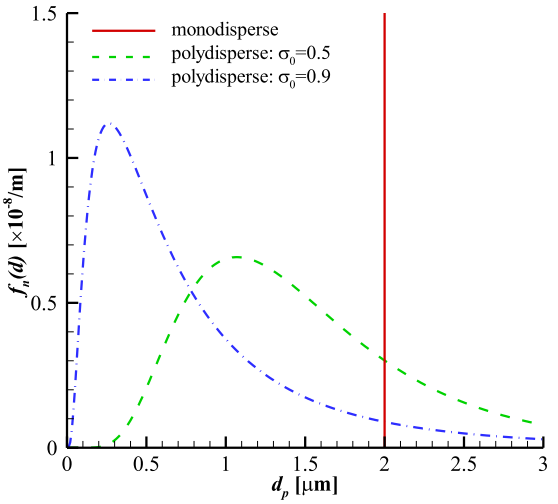

Fig. 15. Log-normal particle size distributions with the nominal diameter $\bar{d} = 2$ μm and different standard deviations.

$$\begin{cases} \bar{d} = \left[\int_0^\infty s^3 f_n(s)ds\right]^{1/3} = d_{nM} e^{\frac{3}{2}\sigma_0^2} \\ \bar{d}_m = \left[\int_0^\infty s^4 f_n(s)ds\right] \Big/ \left[\int_0^\infty s^3 f_n(s)ds\right] = d_{nM} e^{\frac{7}{2}\sigma_0^2}, \end{cases} \tag{48}$$

which yields $d_{nM} = 1.37$ μm and $\sigma_0 = 0.5$. The size distribution of this test material is shown in Fig. 15 by the number frequency distribution function defined in Eq. (46). For comparison, the log-normal distribution with fixed $\bar{d} = 2$ μm but larger $\sigma_0 = 0.9$ is presented in Fig. 15 as well.

6.4.2. 1D case

The same condition of the monodisperse 2-μm Al-air detonation case in Section 6.2 is simulated here, but with two log-normal particle size distributions: one as in Zhang et al. [9] with $\sigma_0 = 0.5$ and the other more widely polydisperse one with $\sigma_0 = 0.9$. Notably, in order to obtain more physics-consistent results, the realistic heat capacities of Al and Al_2O_3 are described as functions of temperature via Eq. (9), instead of constant values. The calculated 1D detonation speeds are equal to $D = 1560$ and 1601 m/s for the polydisperse Al-air suspensions with $\sigma_0 = 0.5$ and 0.9, respectively, while the peak pressures are $p_{\max}/p = 26.85$ and 26.81, respectively. Compared with the results of the monodisperse counterpart in Section 6.2, the detonation speed and peak pressure change to a limited extent even with a continuous particle size distribution. This finding is consistent with the conclusions drawn in [8,57].

The detailed 1D polydisperse Al-air detonation front structures with $\sigma_0 = 0.5$ and 0.9 at $t = 2$ ms are shown in Fig. 16, with the coordinate x originating at the detonation front. The results of the monodisperse counterpart are also available here for comparison. One important characteristic shown in Figs. 16(a)–(d) is that most features of monodisperse Al-air detonations, including the double peaks in gas pressure, density and velocity profiles and the kink in gas temperature profile, as shown by the red lines in Fig. 16, disappear in polydisperse detonations. There is only a single peak for every gas quantity in the detonation fronts, and the changes of these quantities after shock compression become smooth, very similar to the wave front structures in gaseous detonations. These differences between polydisperse and monodisperse detonations are mainly attributed to the multiple time and length scales in polydisperse suspensions with continuous particle size distributions. A future study with in-depth analyses is needed to further explain the mechanisms of polydisperse detonations.

Nevertheless, any effect that occurs in the post-shock-front zone (before the C-J plane), especially combustion of fuels and other interphase interactions in two-phase mixtures, is of great importance to the propagation of the detonation wave. Therefore, differences in detonation front structures, observed by introducing realistic particle size distributions, should exert great influences on two-phase detonation researches, such as instabilities, initiations, DDT processes, detonation preventions and so on, which rises the great demand of developing the new Eulerian-Lagrangian method to conduct polydisperse detonation simulations.

6.4.3. 2D detonation cell structure

As known, the detonation cell size is greatly influenced by the characteristic length of reaction zone [43,59]. In Fig. 16(e), the reaction zones of polydisperse detonations are shown significantly larger than that of the monodisperse counterpart, which will lead to different detonation cell sizes. The comparisons of the cellular detonations between the monodisperse Al-air suspension with a uniform 2-μm particle diameter and the polydisperse Al-air suspensions with $\bar{d} = 2$ μm and $\sigma_0 =$

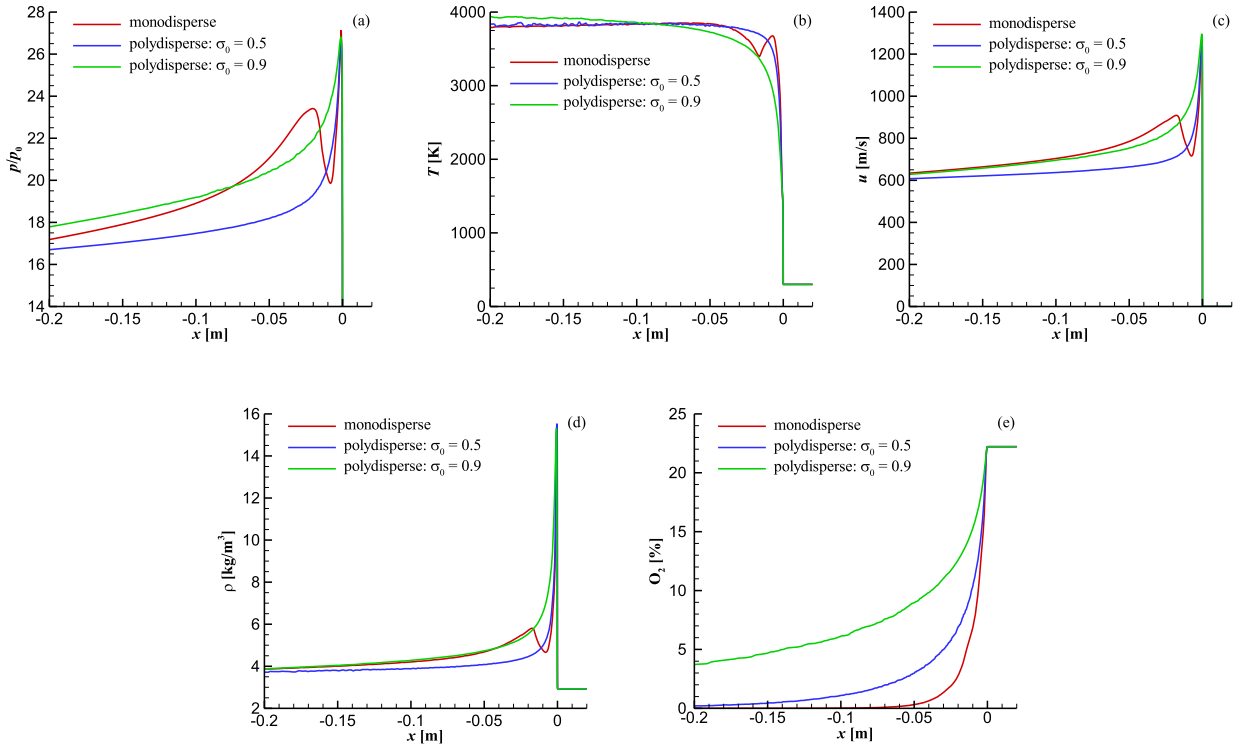

Fig. 16. Comparisons of front structures in gas phase of polydisperse and monodisperse Al-air detonations: (a) pressure, (b) temperature, (c) velocity, (d) density and (e) mass fraction of O_2.

0.5 or 0.9 are shown in Fig. 17 by peak pressure contours. The estimated cell sizes of the monodisperse detonation and the polydisperse detonations with $\sigma_0 = 0.5$ and 0.9 are $\lambda = 10.5 \pm 0.5$ mm, 13.3 ± 0.8 mm and 22.2 ± 2.2 mm, respectively. $\lambda_{polydisperse}$ is 27% larger for $\sigma_0 = 0.5$ and even 111% larger for $\sigma_0 = 0.9$ than $\lambda_{monodisperse}$. The order of detonation cell sizes for the monodisperse and polydisperse detonations are consistent with the order of the lengths of combustion zones depicted in Fig. 16(e).

Because the cellular structures reflect the multidimensional stabilities of detonation wave propagation, the precise predictions of detonation cellular structures are essential to the understanding of the mechanisms of detonation waves propagating in multidimensional spaces and to the prevention of explosion hazards [44]. It should be noted that, many experimental-consistent detonation cell size simulation results are achieved by adjusting some key combustion parameters. The current results draw the attention of taking the polydisperse distribution of particles in the two-phase mixtures into consideration, which also reflects the importance of conducting simulations under the Eulerian-Lagrangian framework.

7. Conclusions

Motivated by the facts that the realistic reactive dust in industries and experiments is always polydisperse in size and the traditional simulation methods developed under the Eulerian-Eulerian framework are of great difficulties in dealing with this kind of gas-particle suspension, in this paper, a numerical code is developed by expanding the original Eulerian CE/SE algorithm into an Eulerian-Lagrangian framework for gas-particle two-phase detonation simulations. Meanwhile, a dynamic data structure with convenient delete, insert and communication operations is introduced to store the information of solid particles and overcome the formidable communication costs associated with using traditional MPI parallelization to accelerate the solution process of two-phase flows under the Eulerian-Lagrangian framework. The code is proved to be of good MPI parallelization performances with such a dynamic data structure.

Three cases of high-speed monodisperse gas/inert particle and gas/reactive particle flows that have been simulated in previous papers [23,24,31] are employed to validate and showcase the capacities of the developed code. The first case is the 1D gas-particle shock tube problem, and the code is proved to be capable of capturing the typical characteristics of heat and momentum exchanges in two-phase high-speed flows. Sequentially, the 1D and 2D gas-particle detonation problems with the hybrid combustion model are simulated. All the results agree well with the previous simulation and experimental results in the reference papers.

Following the validation of the numerical algorithm, comparisons between the monodisperse and polydisperse gas-particle detonations with log-normal particle size distributions were conducted. It is found that the 1D detonation front structures are quite different. Many two-phase detonation features, identified in monodisperse cases, disappear in poly-

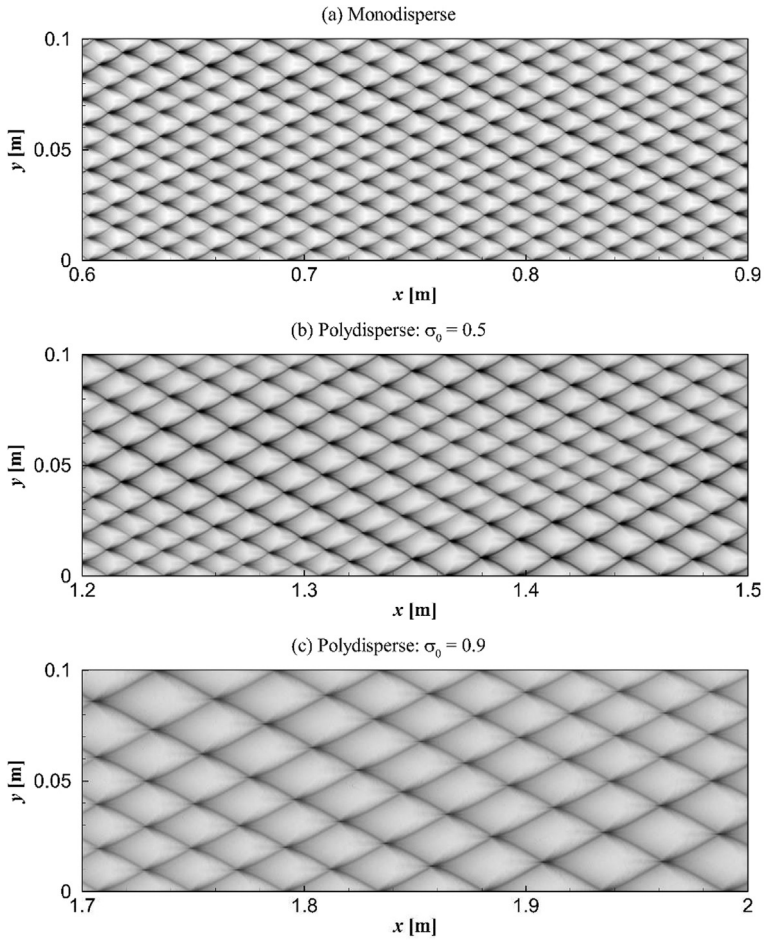

Fig. 17. Comparisons of cellular detonations (peak pressure contours) of Al-air mixtures, (a) monodisperse with $d_p = 2$ μm, and polydisperse with (b) $\sigma_0 = 0.5$ and (c) $\sigma_0 = 0.9$.

disperse cases, and the polydisperse detonation front structures are similar to those of purely gaseous detonations. These differences are expected to result in different propagation and development characteristics of gas-particle detonations. Moreover, the reaction zones are larger in polydisperse cases, which yield larger detonation cell sizes consequently. For the case of polydisperse detonation with $\sigma_0 = 0.9$, the detonation cell size is even twice larger than those predicted in monodisperse detonation. In other words, the particle size distributions have effects on the multidimension stabilities of gas-particle detonations. The importance of considering particle size distribution in realistic gas-particle detonation modeling and simulating this type of flows under an Eulerian-Lagrangian framework is clearly demonstrated.

To improve the code capabilities regarding gas-particle detonation simulations, the future work will be focused on the inclusion of detailed chemistry to model the combustion of reactive particles similar to those in Liang et al. [60]. Moreover, in-depth analyses need to be done to understand the mechanisms of realistic polydisperse gas-particle detonations.

Acknowledgements

This work was supported by the National Natural Science Foundation of China (Grant Nos. 11672312, 11772284 and 11532014), the Research Grants Council, University Grants Committee, Hong Kong (Grant No. 152151/16E), the Department of Mechanical Engineering, The Hong Kong Polytechnic University (Grant No. G-YBYJ) and the opening project of State Key Laboratory of Explosion Science and Technology, Beijing Institute of Technology (Grant No. KFJJ18-12M).

References

[1] T. Abbasi, S.A. Abbasi, Dust explosions-Cases, causes, consequences, and control, J. Hazard. Mater. 140 (2007) 7–44.
[2] J. Bouillard, A. Vignes, O. Dufaud, L. Perrin, D. Thomas, Ignition and explosion risks of nanopowders, J. Hazard. Mater. 181 (2010) 873–880.
[3] B. Veyssiere, Detonations in gas-particle mixtures, J. Propuls. Power 22 (2006) 1269–1288.
[4] J.C. Melcher, H. Krier, R.L. Burton, Burning aluminum particles inside a laboratory-scale solid rocket motor, J. Propuls. Power 18 (2002) 631–640.

[5] L. Meda, G. Marra, L. Galfetti, F. Severini, L.D. Luca, Nono-aluminum as energetic material for rocket propellants, Mat. Sci. Eng. C, Mater. 27 (2007) 1393–1396.
[6] G.D. Roy, S.M. Frolov, A.A. Borisov, D.W. Netzer, Pulse detonation propulsion: challenges, current status, and future perspective, Prog. Energy Combust. Sci. 30 (2004) 545–672.
[7] F. Zhang, H. Grönig, Two-headed detonation in reactive particle-oxidizing gas flow, Phys. Fluids A 4 (1992) 2308–2315.
[8] F. Zhang, H. Grönig, A. van de Ven, DDT and detonation waves in dust-air mixtures, Shock Waves 11 (2001) 53–71.
[9] F. Zhang, S.B. Murray, K.B. Gerrard, Aluminum particles-air detonation at elevated pressures, Shock Waves 15 (2006) 313–324.
[10] B. Veyssiere, Structure of the detonations in gaseous mixtures containing aluminum particles in suspension, in: Dynamics of Explosions, in: Progress in Astronautics and Aeronautics, vol. 106, AIAA, New York, 1986, pp. 522–544.
[11] A.A. Borisov, B.A. Khasainov, E.L. Saneev, I.B. Fomin, S.V. Khomik, B. Veyssiere, On the detonation of aluminum suspensions in air and in oxygen, in: A.A. Borisov (Ed.), Dynamic Structure of Detonation in Gaseous and Dispersed Media, Springer, Dordrecht, 1991, pp. 215–253.
[12] W. Ingignoli, B. Veyssiere, B.A. Khasainov, Study of detonation initiation in unconfined aluminum dust clouds, in: G.D. Roy, S.M. Frolov, K. Kailasanath, N.N. Smirnov (Eds.), Gaseous and Heterogeneous Detonations: Science to Applications, ENAS Publishers, Moscow, 1999, pp. 337–350.
[13] R. Friedman, A. Maček, Ignition and combustion of aluminium particles in hot ambient gases, Combust. Flame 6 (1962) 9–19.
[14] M.W. Beckstead, A Summary of Aluminum Combustion, Report No. RTO-EN-023, Brigham Young University, USA, 2002.
[15] B. Veyssiere, B.A. Khasainov, A model for steady, plane, double-front detonations (DFD) in gaseous explosive mixtures with aluminum particles in suspension, Combust. Flame 85 (1991) 241–253.
[16] B. Veyssiere, B.A. Khasainov, A. Briand, Investigation of detonation initiation in aluminum suspensions, Shock Waves 18 (2008) 307–315.
[17] A. Davis, Solid propellants: the combustion of particles of metal ingredients, Combust. Flame 7 (1963) 227–234.
[18] T. Bazyn, H. Krier, N. Glumac, Oxidizer and pressure effects on the combustion of 10-micron aluminum particles, J. Propuls. Power 21 (2005) 577–582.
[19] A.E. Medvedev, A.V. Fedorov, V.M. Fomin, Description of ignition and combustion of gas mixtures with solid particles by methods of the mechanics of continuous media, Combust. Explos. Shock Waves 20 (1984) 127–132.
[20] A.V. Fedorov, Structure of the heterogeneous detonation of aluminum particles dispersed in oxygen, Combust. Explos. Shock Waves 28 (1992) 277–286.
[21] A.V. Fedorov, T.A. Khmel', Mathematical modeling of detonation of an aluminum dust in oxygen with allowance for velocity nonequilibrium of the particles, Combust. Explos. Shock Waves 33 (1997) 695–704.
[22] A.V. Fedorov, T.A. Khmel', Numerical simulation of formation of cellular heterogeneous detonation of aluminum particles in oxygen, Combust. Explos. Shock Waves 41 (2005) 435–448.
[23] F. Zhang, K. Gerrard, Reaction mechanism of aluminum-particle-air detonation, J. Propuls. Power 25 (2009) 845–858.
[24] A. Briand, B. Veyssiere, B.A. Khasainov, Modelling of detonation cellular structure in aluminium suspensions, Shock Waves 20 (2010) 521–529.
[25] H.H. Teng, Z.L. Jiang, Numerical simulation of one-dimensional aluminum particle–air detonation with realistic heat capacities, Combust. Flame 160 (2013) 463–472.
[26] B. Veyssiere, B.A. Khasainov, Structure and multiplicity of detonation regimes in heterogeneous hybrid mixtures, Shock Waves 4 (1995) 171–186.
[27] B.A. Khasainov, B. Veyssiere, Initiation of detonation regimes in hybrid two-phase mixtures, Shock Waves 5 (1996) 9–15.
[28] F. Durst, D. Milojevic, B. Schönung, Eulerian and Lagrangian predictions of particulate two-phase flows: a numerical study, Appl. Math. Model. 8 (1984) 101–115.
[29] N.A. Patankar, D.D. Joseph, Modeling and numerical simulation of particulate flows by the Eulerian-Lagrangian approach, Int. J. Multiph. Flow 27 (2001) 1659–1684.
[30] O. Igra, G. Ben-Dor, Dusty shock waves, Appl. Mech. Rev. 41 (1988) 379–437.
[31] T. Saito, M. Marumoto, K. Takayama, Numerical investigations of shock waves in gas-particle mixtures, Shock Waves 13 (2003) 299–322.
[32] S.C. Chang, W.M. To, A New Numerical Framework for Solving Conservation Laws – The Method of Space-Time Conservation Element and Solution Element, NASA TM 104495, August 1991.
[33] S.C. Chang, X.Y. Wang, C.Y. Chow, New Development in the Method of Space-Time Conservation Element and Solution Element – Applications to Two-Dimensional Time-Marching Problems, NASA TM 106758, December 1994.
[34] S.C. Chang, The method of space-time conservation element and solution element – a new approach for solving the Navier-Stokes and Euler equations, J. Comput. Phys. 119 (1995) 295–324.
[35] S.T. Yu, S.C. Chang, Treatments of stiff source terms in conservation laws by the method of space-time conservation element/solution element, in: 35th AIAA Aerospace Sciences Meeting and Exhibit, 1997, AIAA Paper 97-0435.
[36] S.C. Chang, X.Y. Wang, C.Y. Chow, The Space-Time Conservation Element and Solution Element Method – A New High-Resolution and Genuinely Multidimensional Paradigm for Solving Conservation Laws, I: The Two-Dimensional Time Marching Schemes, NASA TM 208843, December 1998.
[37] X.Y. Wang, S.C. Chang, A 2D non-splitting unstructured triangular mesh Euler solver based on the space-time conservation element and solution element method, Comput. Fluid Dyn. J. 8 (1999) 309–325.
[38] X.Y. Wang, S.C. Chang, A 3D structured/unstructured Euler solver based on the space-time conservation element and solution element method, in: A Collection of Technical Papers, 14th AIAA CFD Conference, June 28–July 1, 1999, Norfolk, Virginia, 1999, AIAA Paper 99-3278.
[39] S.C. Chang, X.Y. Wang, C.Y. Chow, The space-time conservation element and solution element method: a new high-resolution and genuinely multidimensional paradigm for solving conservation laws, J. Comput. Phys. 156 (1999) 89–136.
[40] Z.C. Zhang, S.T. John Yu, S.C. Chang, A space-time conservation element and solution element method for solving the two- and three-dimensional unsteady Euler equations using quadrilateral and hexahedral meshes, J. Comput. Phys. 175 (2002) 168–199.
[41] S.J. Park, S.T. Yu, M.C. Lai, S.C. Chang, P.C.E. Jorgenson, Numerical calculation of unstable detonations by the method of space-time conservation element and solution element, in: 37th AIAA Aerospace Sciences Meeting and Exhibit, 1999, AIAA Paper 99-0491.
[42] B. Wang, H. He, S.T. John Yu, Direct calculation of wave implosion for detonation initiation, AIAA J. 43 (2005) 2157–2169.
[43] L.S. Shi, H. Shen, P. Zhang, D.L. Zhang, C.Y. Wen, Assessment of vibrational non-equilibrium effect on detonation cell size, Combust. Sci. Technol. 189 (2017) 841–853.
[44] H. Shen, M. Parsani, The role of multidimensional instabilities in direct initiation of gaseous detonations in free space, J. Fluid Mech. 813 (2017) R4.
[45] H. Shen, C.Y. Wen, D.L. Zhang, A characteristic space-time conservation element and solution element method for conservation laws, J. Comput. Phys. 288 (2015) 101–118.
[46] H. Shen, C.Y. Wen, A characteristic space-time conservation element and solution element method for conservation laws, II: multidimensional extension, J. Comput. Phys. 305 (2016) 775–792.
[47] H. Shen, C.Y. Wen, M. Parsani, C.W. Shu, Maximum-principle-satisfying space-time conservation element and solution element scheme applied to compressible multifluids, J. Comput. Phys. 330 (2017) 668–692.
[48] C.Y. Wen, H.S. Massimi, H. Shen, Extension of CE/SE method to non-equilibrium dissociating flows, J. Comput. Phys. 356 (2018) 240–260.
[49] H. Shen, C.Y. Wen, K.X. Liu, D.L. Zhang, Robust high-order space-time conservative schemes for solving conservation laws on hybrid meshes, J. Comput. Phys. 281 (2015) 375–402.
[50] G. Wang, D.L. Zhang, K.X. Liu, J.T. Wang, An improved CE/SE scheme for numerical simulation of gaseous and two-phase detonations, Comput. Fluids 39 (2010) 168–177.

[51] G. Wang, H.Y. Zhu, Q.H. Sun, D.L. Zhang, K.X. Liu, An improved CE/SE scheme and its application to dilute gas-particle flows, Comput. Phys. Commun. 182 (2011) 1589–1601.
[52] B.J. McBride, M.J. Zehe, S. Gordon, NASA Glenn Coefficients for Calculating Thermodynamic Properties of Individual Species, NASA/TP, Report No. 2002-211556, 2002.
[53] D.L. Ropp, J.N. Shadid, Stability of operator splitting methods for systems with indefinite operators: advection-diffusion-reaction systems, J. Comput. Phys. 228 (2009) 3508–3516.
[54] J.T. Wang, K.X. Liu, D.L. Zhang, An improved CE/SE scheme for multi-material elastic-plastic flows and its applications, Comput. Fluids 38 (2009) 544–551.
[55] K.C.K. Uy, L.S. Shi, C.Y. Wen, Prediction of half reaction length for H_2–O_2–Ar detonation with an extended vibrational nonequilibrium Zel'dovich–von Neumann–Döring (ZND) model, Int. J. Hydrog. Energy 44 (2019) 7667–7674.
[56] S.E. Olsen, M.W. Beckstead, Burn time measurements of single aluminum particles in steam and CO_2 mixtures, J. Propuls. Power 12 (1996) 662–671.
[57] K. Benkiewicz, A.K. Hayashi, Parametric studies of an aluminum combustion model for simulations of detonation waves, AIAA J. 44 (2006) 608–619.
[58] C.T. Crowe, J.D. Schwarzkopf, M. Sommerfeld, Y. Tsuji, Multiphase Flows with Droplets and Particles, 2nd edition, CRC Press LLC, 2012, pp. 39–56.
[59] A.I. Gavrikov, A.A. Efimenko, S.B. Dorofeev, A model for detonation cell size prediction from chemical kinetics, Combust. Flame 120 (2000) 19–33.
[60] Y. Liang, M.W. Beckstead, Numerical simulation of quasi-steady, single aluminum particle combustion in air, in: 36th Aerospace Sciences Meeting and Exhibit, 1998, AIAA 1998-0254.